The Large–scale and Small–scale Clustering of Lyman–Break Galaxies at $3.5 \leq z \leq 5.5$ from the GOODS survey

Kyoung-Soo Lee[1,2], Mauro Giavalisco[2], Oleg Y. Gnedin[3], Rachel S. Somerville[2,4], Henry C. Ferguson[2], Mark Dickinson[5], Masami Ouchi[2,6]

ABSTRACT

We report on the angular correlation function of Lyman–break galaxies (LBGs) at $z \sim 4$ and ~ 5 from deep samples obtained from the Great Observatories Deep Origins Survey (GOODS). As for LBGs at $z \sim 3$, the shape of $w(\theta)$ of the GOODS LBGs is well approximated by a power–law with the slope $\beta \approx 0.6$ at angular separation $\theta \geq 10$ arcsec. The clustering strength of $z \sim 4$, 5 LBGs depends on the rest–frame UV luminosity similar to that of $z \sim 3$ ones, with brighter galaxies more strongly clustered than fainter ones. At smaller separations, $w(\theta)$ significantly exceeds the extrapolation of the large–scale power–law fit, implying enhanced spatial clustering on comoving scales $r \leq 1$ Mpc. We also find that bright LBGs statistically have more faint companions on scales $\theta \lesssim 20$ arcsec than fainter ones. The enhanced small–scale clustering is very likely due to sub–structure, reflecting multiple galaxies within the same massive halos. A simple model for the halo occupation distribution along with the halo mass function in a ΛCDM cosmology, reproduces well the observed $w(\theta)$. The scaling relationship of the clustering strength with volume density and with redshift is quantitatively consistent with that of CDM halos. If we associate LBGs with dark matter halos that have the same clustering strength, this luminosity dependence of $w(\theta)$ implies a close correlation between the halo mass and the star formation rate. A comparison of the clustering strength of three samples of equal luminosity limit at $z \sim 3$, 4 and 5 shows that the LBGs at $z \sim 5$ are hosted

[1]Johns Hopkins University, Baltimore, MD 21218

[2]Space Telescope Science Institute, Baltimore, MD 21218

[3]Ohio State University, Columbus, OH 43210

[4]Max-Planck-Institut für Astronomie, Heidelberg, Germany

[5]National Optical Astronomy Observatory, Tucson, AZ 85719

[6]Hubble fellow

in halos about 5 – 10 times less massive than those at $z \sim 3 - 4$, suggesting that star–formation was more efficient at $z \sim 5$.

Subject headings: cosmology: observations — galaxies: distances and redshifts — galaxies: evolution — galaxies: formation

1. Introduction

In the current theoretical framework of galaxy evolution, the observed spatial clustering of galaxies is interpreted as reflecting the clustering of the dark matter halos that host them. Galaxies of different luminosity, spectral type, morphology, etc. are observed to have, in general, different clustering properties, because the specific criteria adopted to select them also select different "types" of halos. For example, because more massive halos have stronger spatial clustering than less massive ones, galaxies selected by criteria that also select the high–end of the halo mass function will be observed to be more clustered than galaxies whose selection criteria correspond to less massive halos. Similarly, the apparent "evolution" of the spatial clustering of galaxies as a function of redshift is interpreted as the result of the specific "mapping" of the selection criteria of the galaxies into a mass range of the halo mass function and of the evolution of the clustering of the halos, which is driven by gravity.

This dependence of galaxy clustering on the selection criteria and how they map into properties of the halos is at the same time bad and good news. It is bad news because it makes it very difficult to use galaxies to infer anything about the evolution of dark matter, and hence about cosmology, unless one knows exactly how to go from galaxies' properties to halos' properties, including taking into account the "astrophysical" evolution of the former, a very complex problem. It is good news because, at least for certain type of galaxies and in some simple cases, one can expect to learn something abut the physical relationship between certain properties of the galaxies and those of the underlying halos, possibly testing some of the key ideas behind our understanding of galaxy evolution.

One important case where the relationship between galaxies and halos is being successfully explored by means of the analysis of the spatial clustering is that of the Lyman–break galaxies. These are star–forming galaxies whose rest–frame UV spectral energy distribution is not severely obscured by dust. This type of source is very effectively selected by means of their broad–band UV colors, constructed from around the 912 Å Lyman limit, the Lyα forest region (pronounced in broad–band photometry at $z \gtrsim 2$), and the otherwise relatively featureless continuum redward of the Lyα line (e.g. Steidel & Hamilton 1993; Steidel et al. 1995; Madau et al. 1995). Using optical passbands, where one can take advantage of the

low sky and of the sensitivity and large area coverage of CCD imagers and spectrographs, the technique is effective at redshifts $2.5 \lesssim z \lesssim 6$. Large surveys of Lyman–break galaxies have been conducted over the past ten years in this redshift range, resulting in large and well controlled samples, including large spectroscopic ones (e.g. Steidel et al. 1999; 2003; Giavalisco et al. 2004; Dickinson et al. 2004; Sawicki & Thompson 2005; Vanzella et al. 2005; E. Vanzella et al., in preparation). These surveys are also well suited for clustering measures.

Lyman–break galaxies have been found to have relatively strong spatial clustering, with a correlation length comparable to that of present–day bright spiral galaxies (Giavalisco et al. 1998; Giavalisco & Dickinson 2001; Porciani & Giavalisco 2002; Adelberger et al. 2005). This has been interpreted as evidence that they are biased tracers of the mass density field (Giavalisco et al. 1998; Adelberger et al. 1998; Giavalisco & Dickinson 2001; Bagla 1998). This means that these galaxies are preferentially hosted in the most massive dark–matter halos (Giavalisco & Dickinson 2001; Foucaud et al. 2003; Adelberger et al. 2005), which have stronger spatial clustering than less massive halos (see, e.g. Mo & White 1996). A key piece of evidence linking the mass of the halo to physical properties of the galaxies came with the discovery that the strength of the spatial clustering of Lyman–break galaxies is a function of their UV luminosity, with brighter galaxies having larger correlation length (Giavalisco & Dickinson 2001; Foucaud et al. 2003; Ouchi et al. 2004; Adelberger et al. 2005; Allen et al. 2005). In the halo interpretation, this is explained if brighter galaxies are, on average, hosted in more massive halos. Since the halo mass function is relatively steep, this also implies that the statistical relationship between mass and UV luminosity must be characterized by a correspondingly small scatter (Giavalisco & Dickinson 2001). Because the UV luminosity of Lyman–break galaxies is powered by star formation, this in turn means that the mass and the star–formation rate are relatively tightly correlated or, in other words, that the halo mass is a primary parameter that controls the star–formation activity of the Lyman–break galaxies as expected in galaxy formation models.

The next logical step is to try to derive the relationship between mass and star–formation rate, thus testing the basic ideas behind the physical models of star–formation in young galaxies (e.g. White & Rees 1978). Furthermore, the dependence of the clustering strength on the UV luminosity (clustering segregation hereafter) contains direct information on the scaling relationship between the halo clustering strength (bias) and the volume density once the galaxy luminosity function is known. Since the shape of this relationship depends on the shape of the power spectrum, the observed clustering segregation can be used to test key predictions of the CDM theory (Giavalisco & Dickinson 2001). To do this, however, information on the halo sub–structure, or the halo occupation distribution function (HOD), is also required (e.g. Bullock et al. 2001, Berlind & Weinberg 2002). This function describes

the likelihood that one halo contains more than one galaxy and how this depends on its mass. Once the HOD and the clustering segregation have been measured, then the relationship between mass and UV luminosity (star–formation rate) can be constrained, and a successful model will have to simultaneously reproduce the observed clustering segregation and UV luminosity function.

In principle, the presence of sub–structure and the HOD function can be constrained by the shape of the angular correlation function and, as we will see later, by the statistics of close pairs of galaxies. In practice, this requires measures with relatively high S/N from large and faint samples, unavailable until recently, since most of the secondary halo–companion galaxies have lower mass than the central galaxy and are thus less luminous on average. Furthermore, large samples covering a sufficiently wide dynamic range in luminosity are necessary to provide a robust measure of the shape of the clustering segregation. Giavalisco & Dickinson (2001) first reported the detection of the clustering segregation and measured its shape but with low S/N. Using a deep sample of LBGs at $z \sim 4$ and 5 obtained with the Subaru telescope and the Suprime camera, Hamana et al. (2004) reported evidence that the angular correlation function of LBGs deviates from a power–law at small angular scales and derived the HOD function to explain the deviation. Using the largest sample of LBGs to date at $z \sim 3$, Adelberger et al. (2005) measured the shape of the angular correlation function at large angular separations with high S/N. Their sample, however, is not deep enough to include halo companion galaxies in appreciable number and detect the effect of sub–structures; they could only set an upper limit of 5% to the number of galaxies in common halos.

In this paper we present a study of the clustering properties of Lyman–break galaxies at $z \sim 4$ and ~ 5 at faint flux levels. We use two deep and relatively large samples obtained with *HST* and ACS during the program of multi–band imaging of the Great Observatories Origins Deep Survey (GOODS). In fact, these ACS samples of B_{435} and V_{606}–band dropouts are currently the largest and the most complete at their depth of such galaxies[1]. Since their size is suitable to measure the angular clustering with high S/N, we have embarked on a project to characterize the physical association between the activity of star formation of the galaxies and the properties of the dark matter halos, primarily the mass, thus providing quantitative tests to the CDM hierarchical theory of galaxy formation. Here we present significantly improved measures of the clustering segregation down to faint flux limits ($z_{850} \sim 27$), show

---

[1]Analogous samples have also been obtained during the Hubble Ultra Deep Field survey, which covers a small portion of the GOODS southern field (CDF–S) with identical passbands as the primary GOODS survey. While significantly deeper than the GOODS samples, the HUDF ones are much smaller in size because of the minimal areal coverage of the HUDF.

direct evidence of sub-structure in halos, and derive the corresponding HOD. We postpone to a following paper the derivation of the relationship between mass and star–formation rate. All magnitudes in this paper are in the AB scale of Gunn & Oke (1975) and, when necessary, we use a cosmology with $\Omega_m = 0.3$, $\Omega_\Lambda = 0.7$, $\sigma_8 = 0.9$, $\Gamma = 0.21$, $H_0 = 100h$ km s^{-1} Mpc^{-1} with $h = 0.7$ and baryonic density $\Omega_b = 0.04$.

2. The Data and The Samples

Deep optical multi–band imaging with *HST* and ACS has been acquired as part of the program of observations of the GOODS. These ACS data consist of a mosaic of images in each of the B_{435}, V_{606}, i_{775} and z_{850} passbands for a total of 3, 2.5, 2.5 and 5 orbits of integration time, respectively, in each of the two GOODS fields. These two fields are centered around the Hubble Deep Field North (HDF–N) and Chandra Deep Field South (CDF–S) and cover approximately $10' \times 17'$ each, for a total area coverage of about 0.1 square degree. To search for supernovae at high redshift (Riess et al. 2004), the observations in the V_{606}, i_{775} and z_{850} bands were not done continuously, but sequenced into "epochs" separated by about 45 days from each other. Because the nominal roll of *HST* changes at a rate of about 1 degree per day, this observing strategy resulted in images acquired during different epochs having position angle in the sky differing by integer multiple of 45 degree. This gives the characteristic jagged edges of the GOODS mosaics in the V_{606}, i_{775} and z_{850} bands. Giavalisco et al. (2004a) present an overall description of the GOODS project, and we refer the reader to that paper for additional details on the ACS observations.

The V_{606}, i_{775} and z_{850}–band mosaics presented in Giavalisco et al. (2004a,b) only include the first 3 epochs of observations stacked together, while the samples of Lyman–break galaxies at $z \sim 4$ and ~ 5 that we are about to discuss here have been extracted from the version v1.0 reduction of the ACS data, which include the full stack of the five epochs. The B_{435}–band mosaic discussed by Giavalisco et al. (2004a), however, already includes all the data, since all the B–band observations were taken continuously. A complete description of the v1.0 ACS images will be presented in an upcoming paper (M. Giavalisco et al., in preparation). Detailed information can also be found in the GOODS website, at the link `http://www.stsci.edu/science/goods/v1_release_readme/h_goods_v1.0_rdm.html`.

We now provide a brief summary of the data reduction and stacking process for the version v1.0 data release. Differently from the version v0.5 public release and from the mosaic discussed in Giavalisco et al. (2004a), for the version v1.0 reduction we have re–processed all the data (including the B_{435}–band images) using the best calibration and reference files available. We have improved treatments of the geometrical distortions of ACS using updated

coefficients together with corrections for the velocity aberration distortion, and we have also improved rejection of cosmic rays and other blemishes. We have stacked the individual exposures together in each band using the drizzling algorithm in two independent phases. In the first phase, images taken in the same filters are sky-subtracted and drizzled onto a common pixel grid at the instrument native scale (0.05 arcsec/pixel). Cosmic rays and deviant pixels are identified during this process and flagged in mask files specifically created for this purpose. Information on detector blemishes (hot pixels, bad columns, etc.) in post–pipeline masks (which have also been drizzled onto the same grid) is included in the new masks at this time. During the second phase, the images and the mask files are blotted back to the original positions, drizzled again onto a common astrometric grid with scale 0.03 arcsec/pixel, and stacked together. During this process corrections for the ACS geometrical distortion are applied, cosmic rays flagged during the previous processing block are masked out from the stack, and additional, low-level cosmic rays and defects are identified and masked, too. The final stacks reach similar 1–σ surface brightness limits for the north and south, which are listed in Table 1.

Multi–band source catalogs, which are public and available at the Web site listed above, have been created using the SExtractor package (Bertin & Arnouts 1996). We made the detections using the z_{850}–band mosaic, and then used a variety of photometric apertures, including isophotal and a suite of circular apertures of varying radius, as "fixed apertures" to carry out matched photometry in all bands. We have measured the completeness of the catalogs as a function of the size and magnitude of the sources through extensive Monte Carlo simulations. In these simulations we have inserted a very large number of model galaxies (169,100) into the ACS mosaic, after convolution with the ACS PSF and after adding the appropriate Poisson and detector noise. We used galaxies with both exponential and $r^{1/4}$ light profiles with random ellipticity and orientation in the sky, with varying apparent magnitude and size, and then retrieved them with identical procedures as for the real galaxies. From these simulations we estimate that the catalogs are $\approx 50\%$ complete at $z_{850}\sim 26.5$ for sources with half–light radius $r_{1/2} \leq 0.2$ arcsec, and about 10% complete at $z_{850}\sim 27$. We have also run multi–band simulations for sources with a given input spectral energy distribution (SED) to test completeness relative to color selection, as we will discuss in a moment.

We have also used deep ground–based multi–wavelength imaging data to select samples of Lyman–break galaxies at redshifts $z \sim 3$ (U–band dropouts) in the CDF–S field, albeit in a larger area than the ACS fields. These data were acquired as part of the program of ancillary observations of the GOODS project. They are also described in Giavalisco et al. (2004a), and we refer the reader to that publication for details. Here we will summarize the key properties of these data. The B and R bands were taken with the Wide Field Imager (WFI) at the 2.2m MPG/ESO telescope, while the U–band observations were carried out

with the MOSAIC II Camera at the CTIO 4m telescope. The stacked image in each band covers a contiguous region of approximately 0.4 degree^2. Some parameters of these ground–based data sets are detailed in Table 2.

Samples of star–forming galaxies at $z \sim 3$, 4 and 5 were photometrically selected using the Lyman Break technique (e.g. Steidel et al. 1999; Madau et al. 1996; Giavalisco et al. 2004b.; see also Giavalisco 2002 for a review). The technique and its application to clustering studies (Giavalisco et al. 1998; Adelberger et al. 1998; Giavalisco & Dickinson 2001) have been extensively discussed in the past, and we refer the reader to the cited literature.

Lyman–break galaxies (LBGs) at $z \sim 4$ and ~ 5, B_{435} and V_{606}–band dropouts, respectively, were extracted from the GOODS v1.0 r1.1 catalogs using the same color selection criteria described by Giavalisco et al. (2004b), which we report here for convenience. We defined the B_{435} and V_{606}–band dropouts as

$$\begin{aligned}
(B_{435} - V_{606}) &\geq 1.2 + 1.4 \times (V_{606} - z_{850}) \wedge \\
(B_{435} - V_{606}) &\geq 1.2 \wedge V_{606} - z_{850} \leq 1.2,
\end{aligned}$$

and

$$\begin{aligned}
(V_{606} - i_{775}) &> 1.5 + 0.9 \times (i_{775} - z_{850}) \vee \\
(V_{606} - i_{775}) &> 2.0 \wedge (V_{606} - i_{775}) \geq 1.2 \wedge \\
(i_{775} - z_{850}) &\leq 1.3,
\end{aligned}$$

where the symbols $\vee$ and $\wedge$ are the logical “OR” and “AND” operators, respectively. In both cases we have limited the apparent magnitude of the samples to $z_{850} \leq 27.0$ for completeness. We have also visually inspected each galaxy included in the samples and removed objects with stellar morphology and obvious spurious detections, such as diffraction spikes. Down to the adopted flux limit of $z_{850} \leq 27.0$, the ACS samples include 2463 B_{435}–band dropouts and 878 V_{606}–band dropouts.

Lyman–break galaxies at $z \sim 3$ were selected using

$$\begin{aligned}
(U - B) &\geq (B - R) + 0.6 \wedge \\
(U - B) &\geq 0.9 \wedge (B - R) \leq 2.5
\end{aligned}$$

This ground–based sample includes 1609 galaxies in the central region of the field which was used for the clustering analysis down to a flux limit of $R \leq 25.5$. The corresponding surface density values of our samples down to the above mentioned flux limits are $\Sigma = 2.7$, 7.7, 2.7 galaxies/arcmin^2 for the U, B_{435} and V_{606}–dropouts, respectively.

Contamination from galactic stars is nearly negligible for the B_{435} and V_{606}–band dropouts because they were morphologically culled taking advantage of the high angular resolution of the GOODS ACS data. For the ground-based sample such culling is not possible; however stellar contamination in high galactic latitude fields such as GOODS has been found to be $\approx 4\%$ in previous spectroscopic surveys (Steidel et al. 1998). We also impose a minimum signal to noise ratio (S/N $\geq$ 10) in order to filter out spurious sources. This also helps (relatively) homogeneous detection of star-forming galaxies up to a certain magnitude limit when dealing with data produced with several separate pointings with overlaps. Even at the cost of losing some fraction of the faintest LBGs, it is desirable for clustering studies to avoid an artificial clustering signature induced by interlopers and inhomogeneity of the data.

3. Simulations

At $z \sim 3$ the selection of Lyman–break galaxies (U–band dropouts) has been characterized in great detail thanks to the systematic spectroscopic identification of thousands of candidates (e.g. Steidel et al. 2003). In particular, this extensive body of work has shown that the Lyman–break technique is very efficient, with a relatively low rate of contamination from low–redshift interlopers, and has yielded the redshift distribution function $N(z)$ associated with a given set of color selection criteria. While spectroscopic identifications have been made of Lyman–break galaxies at $z \sim 4$ and ~ 5 (Steidel et al. 1999; Giavalisco et al. 2004), including a number presented in this work (see later), the spectroscopic samples still remain too small for accurate measures of the redshift distribution function associated with a specific color selection. Fortunately, as the $z \sim 3$ case has demonstrated (Steidel et al. 1999), Monte Carlo simulations are very effective in providing robust estimates of $N(z)$, which are needed to derive the real–space clustering from the angular one and to measure the galaxies' volume density.

The simulations consists of creating artificial LBGs over a large redshift range (we used $2 \leq z \leq 8$) with assumed distribution functions of UV luminosity, SED, morphology and size, inserting them in the real images with random orientations and inclinations and with the appropriate amount of photon noise, detecting them, and measuring their "observed" photometry and morphology as if they were real galaxies. We have adjusted the input distribution functions of UV luminosity (UV luminosity function), size and SED so that the observed distribution functions of apparent magnitude, UV colors and size of the simulated galaxies best reproduce the same quantities of the real galaxies. Specifically, we used galaxies with exponential and $r^{1/4}$ light profile in equal proportions and size extracted from a log–normal distribution function, as described by Ferguson et al. (2004). This method was first

used by Giavalisco et al. (2004b) and Ferguson et al. (2004); its application to the measure of the UV luminosity function of LBGs will be further discussed in an upcoming paper (M. Giavalisco et al., in preparation).

The average redshifts obtained from the simulations are $z = 3.2 \pm 0.3$, 3.8 ± 0.3, 4.9 ± 0.3 for the U, B_{435} and V_{606}–band dropouts, respectively. Figure 1 shows the redshift distribution $N(z)$ of simulated LBGs together with that of a subset of LBGs with spectroscopic redshifts.

4. Measuring the clustering properties of Lyman–break Galaxies

We now discuss the measure of angular and real–space clustering of LBGs and other clustering properties that we have carried out from our samples. The primary measure is that of the angular correlation function $w(\theta)$, which we deproject with the Limber transform using the redshift distribution function estimated from the simulations (but see later for a discussion on our spectroscopic observations) to derive the real–space correlation length, in the power–law approximation. In our faint samples, the angular correlation function is very well approximated by a power law at large angular separations, roughly $\theta > 10$ arcsec, but it exceeds the extrapolation of the large–scale power–law fit at small scales. To understand the nature of this excess clustering, which is not observed in bright samples, either our own U–band dropout sample or even larger ones (e.g. Adelberger et al. 2005), we have carried out an analysis of the mean number of close neighbors around both bright and faint galaxies. We have used the halo occupation distribution (HOD) formalism to predict the shape of $w(\theta)$ and compare it with our measure.

4.1. The angular correlation function

The inversion of the angular correlation function is a robust method to derive the real–space correlation length if the redshift distribution function is well known (see Giavalisco et al. 1998; Giavalisco & Dickinson 2001; Adelberger et al. 2005). The measure of $w(\theta)$ is relatively straightforward; however some care is required in the analysis of the random errors, and, above all, of systematic errors, since they can significantly bias the result. Given the relatively small area covered by the GOODS fields and the way the observations have been obtained, the two most significant sources of systematic errors are cosmic variance (the integral constraint bias) and sensitivity fluctuation in the survey, which can mimic a spurious clustering signal. These will be discussed separately in dedicated subsections.

We have estimated the angular correlation function using the estimator proposed by

Landy and Szalay (1993):

$$w_{obs}(\theta) = \frac{DD(\theta) - 2DR(\theta) + RR(\theta)}{RR(\theta)}, \tag{1}$$

where $DD(\theta)$ is the number of pairs of observed galaxies with angular separations in the range $(\theta - \delta\theta/2, \theta + \delta\theta/2)$, $RR(\theta)$ is the analogous quantity for random catalogs with the same geometry as the observed catalog and $DR(\theta)$ is the number of random galaxy cross pairs. We have chosen logarithmic binning of the angular separations to provide adequate sampling at small scales while avoiding excessively fine sampling at large scales which would have resulted had linear binning been adopted. We have repeated the measures using 4 different (logarithmic) binsizes for each sample.

To account for the random errors, we have estimated the error bars for each angular bin by bootstrap resampling of the data (e.g. Benoist et al. 1996, Ling, Barrow & Frenk 1986). We have computed values of $w(\theta)$ from 100 randomly selected subsets of galaxies and then used the standard deviation of $w(\theta)$ as our primary error estimate. This method, however, only accounts for random errors appropriate to our sample size, and does not include the uncertainty due to the finite size of our samples, because we use the observed galaxies for the error estimate. In other words, the bootstrap method fails to account for fluctuations on scales larger than our survey. We have used Monte Carlo simulations to estimate these fluctuations of $w(\theta)$ due to cosmic variance and validate our accounting of random errors. We have created a large number of realizations (50) of GOODS samples at $z \sim 4$ and ~ 5 extracted from a population with the same large–scale clustering properties (i.e. surface density and angular correlation function— see Porciani & Giavalisco 2002 for a description of the method) as the observed galaxies. Since the goal of this test is to estimate the uncertainty induced in the observed $w(\theta)$ by the large–scale fluctuations of the density field of the parent population of galaxies from which are samples are extracted from, neglecting the small–scale clustering is inconsequential. Each realization simulates an area of the sky of 1 degree^2 within which we have selected the mock "GOODS" samples of LBGs. We have measured $w(\theta)$ in each sample, and derived the standard deviation of the 50 measures at each angular bin and used it as an estimate of the error bar, finding consistent results with the bootstrap method.

To test the dependence of the angular clustering on the luminosity of the galaxies, we have measured the correlation function for various magnitude cuts in each sample. For the B_{435} and V_{606}–band dropout samples we have defined sub–samples at $z_{850} \leq$ 27.0, 26.5 and 26.0; for the U–band dropouts we have used $R \leq 25.5, 24.5$ and 24.0. In what follows, we will denote each sub–sample as B(V)270, 265, 260 and U255, 245, 240, respectively. The number of galaxies included in each sub–sample is 2463, 1410 and 858 for the B_{435}–band

dropouts, 878, 407 and 218 for the V_{606}–band dropouts, and 1609, 1050 and 554 for the U–band dropouts.

4.2. Correction for sensitivity variations

A possible source of systematic error in surveys such as GOODS, which consist of either mosaics of images (the ACS images) or images taken with CCD mosaics (the ground–based images), is fluctuations of sensitivity across the surveyed area. Such fluctuations, which typically occur on scales that are a fraction of the linear size of the survey, can be sufficiently strong to mimic the presence of clustering and bias the measures of $w(\theta)$.

To estimate this effect in LBGs samples is not straightforward, because these are color–selected as well as flux-limited, and thus the final selection function is a nontrivial function of sensitivity variations in all the different passbands used in the color selection as well as of their respective limiting magnitudes. The best way to take all of these factors into account is to use Monte Carlo simulations. We have generated over 100,000 artificial U and B_{435}–band dropouts and placed them at random positions in each of the U, B, R and B_{435}, V_{606}, i_{775}, z_{850} images of the ground–based and ACS survey, respectively (see above for a description of the simulation technique). We have subsequently "detected" the artificial galaxies and subjected them to the same color selection as if they were real U or B_{435}–band dropouts. To the extent that this process is a faithful representation of the overall selection function of the survey, the spatial distribution of these color–selected mock galaxies will reflect various systematics including the sensitivity variations across the field, the effects of holes due to saturated sources or large seeing (of our ground–based mosaics), to the applied color–selection and so forth.

The correction factor can be estimated by measuring the angular correlation function, $w_{sim}(\theta)$, against a purely random distribution with the same geometry (this should be essentially zero for perfectly homogeneous data). Since $w(\theta)$ is the excess probability of finding a pair, our previous measurement can be corrected as

$$1 + w_{corr}(\theta) = \frac{1 + w_{raw}(\theta)}{1 + w_{sim}(\theta)} \tag{2}$$

where w_{raw} is the measurement using the LS estimator, w_{sim} is the correlation function of artificial galaxies and w_{corr} is the corrected angular correlation function of the dropouts. While the correction is non-negligible at small scales for the U–dropouts, it has negligible effect on the ACS data, hence the correction is applied only to the U–dropout measurement. The subscript of $w_{corr}(\theta)$ will be dropped hereafter unless stated otherwise.

4.3. Integral Constraint

Due to the finite size of any given survey, the correlation function measured from a sample is underestimated by a constant known as the integral constraint, referred to as IC hereafter:

$$\omega_{true}(\theta) = \omega_{obs}(\theta) + IC \tag{3}$$

Since the measure of $w(\theta)$ is underestimated by the same amount on all scales, this also leads to an overestimate of the correlation slope, β. This can be estimated by doubly integrating ω_{true} over the survey area (Roche & Earles 1999).

$$\begin{aligned} IC &= \frac{1}{\Omega^2}\int_1\int_2 \omega_{true}(\theta) d\Omega_1\Omega_2 \\ &= \frac{\Sigma_i RR(\theta_i)\omega_{true}(\theta_i)}{\Sigma_i RR(\theta_i)} = \frac{\Sigma_i RR(\theta_i) A_\omega \theta_i^{-\beta}}{\Sigma_i RR(\theta_i)} \end{aligned} \tag{4}$$

Note that the integral constraint depends on both the size of a given survey (Ω) and the galaxy power spectrum (approximated by a power–law ; A_w and β). However, once the correlation slope β is fixed, IC/A_w only depends on the size and the shape of the survey area. Therefore, one needs to make robust estimate of β from the observational data, then for a fixed β, IC/A_w can be estimated. We calculate the ICs from random catalogs generated over a field with the same size and the geometry as our survey area with a range of A_ω and β. For each set (A_w, β) we calculate IC value using Equation (4) and compute the χ^2 of the measured $w_{obs}(\theta)$. Once β and IC/A_w are robustly measured from the full sample, for other flux–limited samples, A_w is the only parameter that needs to be fitted as $w_{model} = A_w(\theta^{-\beta} - (IC/A_w)_0)$ provided that β does not change significantly with samples of different flux limits. This helps to make reliable measures of the amplitude A_w for sub–samples that have lower signal–to–noise than the full sample.

For the B270 sample, we find that a set (A_w, β, IC) = (0.31, 0.6, 0.012) best describes the measures, however, it should be noted that there is degeneracy between A_w and β. In other words, there is a range of acceptable A_ws and βs for a fixed IC value even for high S/N data, and hence one needs to somewhat arbitrarily fix the slope within the given range. We fix $\beta = 0.6$ and $IC/A_w = 0.039$ for all B_{435} and V_{606}–band dropout samples. Similarly, for the U–band dropouts, we find (A_w, β, IC) = (0.50, 0.6, 0.012) thus $IC/A_w = 0.024$. Note that IC/A_w is much smaller for the U–band dropouts due to the larger field size. On the other hand, the IC values for the full sample of the B_{435} and U–band dropouts are comparable, because the faint ACS B_{435} and V_{606} dropout samples are less clustered (i.e. smaller A_w) than the brighter ground–based sample. Using this method, we find $IC = 0.012$, 0.024, 0.031

for the U255, U245 and U240 sample, $IC = 0.012$, 0.020, 0.027 for the B270, B265 and B260 sample and $IC = 0.024$, 0.031, 0.043 for the V270, V265 and V260 sample, respectively.

When the slope is allowed to vary, the procedure becomes iterative because the derived IC depends on $w(\theta)$ and vice versa, and one cannot conveniently set IC/A_w to be a constant for the fitting. As Adelberger et al. (2005) pointed out, this is often very unstable regardless of the initial guess. Therefore, as a consistency check we estimated the IC using an alternate method suggested by Adelberger et al. (2005). Their method takes advantage of the fact that matter fluctuations, σ^2_{CDM} within a given survey volume are in the linear regime and can be estimated from the power spectrum with an appropriate window function that accounts for the geometry of the survey volume (see their Equation 20). By definition, IC, the variance of density fluctuation of galaxies is $IC \approx b^2\ \sigma^2_{CDM}$. We estimate the galaxy bias, b, from the correlation function itself by using the relation $b = \sigma_{8,g}/\sigma_8(z)$, where $\sigma_{8,g}$ is the galaxy variance in spheres of comoving radius 8 h^{-1} Mpc (Peebles 1980, Equation [59.3]):

$$\sigma^2_{8,g} = \frac{72(r_0/8h^{-1}Mpc)^\gamma}{(3-\gamma)(4-\gamma)(6-\gamma)2^\gamma} \tag{5}$$

where r_0 is the correlation length inferred from the angular correlation function (see next subsection), $\gamma = \beta + 1$ and $\sigma_8(z)$ is the linear matter fluctuation on the same scale extrapolated from $\sigma_8(0) = 0.9$.

When using this method, we find values of both IC and β that are consistent with the previous method, but the IC values are slightly smaller in most cases. For example, for the B270 sample, we find $IC = 0.010$ instead of 0.012, for B265 0.018 instead of 0.020, which makes little difference in the fitted A_w or β values. This may imply that the generic correlation function slope β may be slightly steeper than the fiducial value 0.6 for some sub–samples as can be seen in Table 3. For a fixed r_0, $\sigma_{8,g}$ declines with the slope γ at $1.5 < \gamma < 2.0$. However, for a fixed γ (or β), both methods are in good agreement.

Since the IC is $w(\theta)$–dependent, power–law fitting and correcting for the IC are in fact simultaneous processes. In each iteration, only the $w_{obs}(\theta)$ measurement with $\theta > 10$ arcsec is used for the power–law fit (to probe large scale structure) because at $\theta < 10$ arcsec there may be significant contribution from highly nonlinear small-scale clustering. Figure 2 shows our results for the full B_{435}–band (left panel) and V_{606}–band (right panel) dropout sample together with the best power–law fit. Clear departure from a pure power–law is apparent in both cases on small scales ($\theta < 10$ arcsec).

We fit the data to a linear function in logarithmic space. To estimate 1σ confidence intervals for the parameters A_w and β, we carried out a large ensemble of random realizations of the measured $w(\theta)$ assuming normal errors, and calculated best–fit parameter values for

each of these synthetic data sets. Because we select randomly among the $w(\theta)$ measures of different binsizes for each realization, the peak values of A_w and β may be slightly different from those derived from the individual $w(\theta)$ measures mentioned in the previous subsection. The fitted values of A_w and β are provided in Table 3.

4.4. The Real–Space Correlation Function $\xi(r)$

We derive the real–space correlation function ξ(r) by inverting $w(\theta)$ using the Limber transform (Peebles 1980). If the real–space correlation function has the form $\xi(r) = (r/r_0)^{-\gamma}$, the angular correlation function also has to be a power–law, $w(\theta) = A_w\theta^{-\beta}$ where $\beta = \gamma - 1$ and A_w is related to $\xi(r)$ as,

$$A_w = Cr_0^{\gamma}\int F(z)D_{\theta}^{1-\gamma}(z)N(z)^2 g(z)dz \times [\int N(z)dz]^{-2}$$

where D_θ is the angular diameter distance and $N(z)$ is the redshift selection function derived from the simulations.

$$\begin{aligned} g(z) &= \frac{H_0}{c}[(1+z)^2(1+\Omega_0 z+\Omega_\Lambda((1+z)^{-2}-1))^{1/2}] \\ C &= \sqrt{\pi}\frac{\Gamma[(\gamma-1)/2]}{\Gamma(\gamma/2)}. \end{aligned}$$

We have used the same $N(z)$ for all the different limiting magnitudes since the simulations indicate little change in the redshift distribution for each case. Note that A_w and β are obtained from the measures at $\theta > 10$ arcsec to be representative of large–scale clustering. It is interesting, however, that if we include the data points at $\theta < 10$ arcsec for the fit and allow β to vary, both A_w and β get overestimated by an amount that changes r_0 very little. For example, for the B270 sample, we obtained the r_0–value of 2.82 ± 0.20 h^{-1} Mpc ($2.81^{+0.22}_{-0.21}$ h^{-1} Mpc) when using the data points at $\theta > 3$ ($\theta > 10$) arcsec. Hence our estimates of r_0 are robust regardless of the fiducial value chosen to be considered as large–scale.

The correlation lengths r_0 derived using this method are listed in Table 3. Two different r_0 values derived from the fits with and without the correlation slope β fixed to a fiducial value 0.60, are consistent with each other within the errors. In the following discussion, we regard the former as our best r_0 values. The best–fit r_0 values range from 2.8 h^{-1} Mpc to 7 h^{-1} Mpc (comoving) depending on the median luminosity of the sub–samples. In each redshift range, brighter samples have larger correlation lengths. We have compared our measures with those from other groups for samples with similar median luminosity and in the same redshift range generally finding good agreement. At $z \sim 3$ Adelberger et al. (2005)

found $r_0 = 4.0 \pm 0.6\ h^{-1}$ Mpc for galaxies with magnitude 23.5$\leq \mathcal{R} \leq$25.5 ($\bar{z} = 2.9$), in good agreement with our $R \leq 25.5$ sample for which we found $r_0 = 4.0 \pm 0.2\ h^{-1}$ Mpc. At $z \sim 4$ and 5, Ouchi et al. (2004) reported $r_0 = 4.1 \pm 0.2$ and $5.9^{+1.3}_{-1.7}\ h^{-1}$ Mpc for their LBGz4s ($i' \lesssim 26$) and LBGz5s ($z' < 25.8$) samples, respectively. Using an LBG template spectrum that reproduces the median UV colors of the samples, we computed that the flux limit of Ouchi et al. (2004) correspond to $z_{850} \lesssim$ 26.0 and 25.8, for which we find $r_0 = 5.1^{+0.4}_{-0.5}$ and $5.30^{+1.1}_{-1.0}\ h^{-1}$ Mpc. While the correlation lengths of the two samples of V_{606}–band dropouts are in good agreement, we noticed that Ouchi et al. reported a lower value than ours for the B_{435}–band dropout sample, although the two measures overlap at the $\approx 1.3\sigma$ level.

5. Results

5.1. Dependence of Clustering strength on Luminosity

A number of authors (Giavalisco & Dickinson 2002; Foucaud et al. 2003; Adelberger et al. 2005; Ouchi et al. 2004) have reported the existence of the clustering segregation with the UV luminosity for the LBGs, namely of the fact that the galaxies with higher UV luminosity have stronger spatial clustering (e.g. larger spatial correlation length) than fainter ones. We have examined the dependence of the clustering strength of our samples on luminosity using several apparent magnitude cuts constructed from the full samples. Apparent magnitude cuts roughly correspond to absolute magnitude cuts because the luminosity–distance changes only by $\approx 20\%$ over the redshift range covered by each of our samples and the redshift selection functions are relatively narrow. Whether or not we fix the correlation slope to a fiducial value of $\beta = 0.6$ (Porciani & Giavalisco 2002), we find that the correlation amplitude A_w, and r_0 accordingly, increases with median luminosity.

The correlation length of the B_{435}–band dropouts increases from $2.8 \pm 0.2\ h^{-1}$ to $3.7 \pm 0.3\ h^{-1}$ to $5.1^{+0.4}_{-0.5}\ h^{-1}$ Mpc with increasing luminosity of the samples (see Tables 3).

Note that the faintest sample of B_{435}–band dropouts, which is our faintest sample at any redshift, reaching absolute magnitude $M_{1700} = -18.52$, also has the smallest correlation length, $r_0 = 2.8\ h^{-1}$ Mpc. A similar trend is also found for the V_{606}–band dropouts. For a fixed absolute luminosity, objects will be fainter at $z \sim 5$ than their counterpart at $z \sim 4$ by 0.6 – 0.7 mag in z_{850}–band due to cosmological dimming. This suggests that the correlation lengths for the B_{435} and V_{606}–band dropouts for a fixed absolute UV luminosity are comparable (see Table 3 for details).

In agreement with previous results, we find that the U–band dropouts also follow a similar trend. For the U255 sample ($R \leq 25.5$) we measure a correlation length $r_0 = 4.0^{+0.2}_{-0.2}$

h^{-1} Mpc, in an excellent agreement with the value reported by Adelberger et al. (2005), 4.0 h^{-1} Mpc for roughly the same magnitude threshold ($\langle R - \mathcal{R} \rangle \sim 0.03$ at $z \sim 3$ using our mean LBG spectrum). The correlation length increases to $r_0 = 7.8^{+0.5}_{-0.6}$ h^{-1} for $R \leq 24.0$. Interestingly, this is comparable to 8 h^{-1} Mpc, the correlation length of a sample of distant–red galaxies (DRGs) found at a slightly lower redshift range (Daddi et al. 2003).

The left three panels of Figure 3 show $w(\theta)$ for the full sample (solid lines) and the brightest sub–samples (dashed lines) for each dropout flavor together with best–fit power–laws. The power–fits when β is fixed to 0.6 are shown for clarity. The right panels show the derived correlation lengths for these samples. All samples show a clear trend that brighter samples are more strongly clustered in real space.

The sub–samples that we have used to measure the clustering segregation are not independent from one another, because the galaxies that comprise the brighter samples also belong to the faintest one thus diluting the weak clustering signal from the faintest galaxies. We have repeated the measures using two mutually independent samples that we built by splitting the full B_{435}–band dropouts sample into two independent magnitude bins, $26.3 < z_{850} \leq 27.0$ and $z_{850} \leq 26.3$ with roughly equal number of galaxies in each bin. For these two samples we have measured $r_0 = 4.0 \pm 0.3$ and $2.3^{+0.5}_{-0.4}$ h^{-1} Mpc, respectively. Note that the correlation length of the faint sample is now smaller than 2.8 ± 0.2 h^{-1} Mpc of the $z_{850} \leq 27.0$ sample, consistent with the luminosity segregation.

Recently, Norberg et al. (2001) and Zehavi et al. (2002) observed luminosity segregation in the optically selected galaxies in local universe with high S/N. Note that a direct comparison between our results and the local ones is not possible, since the UV luminosity is powered by star formation rate, while the optical luminosity is mostly powered by stellar mass. However, understanding how UV luminosity scales with the clustering strength, at both high and low luminosities, will shed light on the relationship between halo mass and star formation rate. Unfortunately, our brightest magnitude cut made to the ACS sample is $z_{850} = 26.0$, which is still more than 1 mag fainter than m^* (m^* is $z_{850} \sim 24.7$ and 24.8 at $z = 4$ and 5; M. Giavalisco et al., in preparation), while the size of our U dropout samples are relatively small due to the shallow depth of our ground–based data sets. We plan to extend our observation of clustering segregation to the higher–luminosity regime at the same redshift intervals ($z \sim 3 – 5$) in a follow–up paper (K.-S. Lee et al., in preparation).

5.2. Small–scale statistics

Our deep ACS data also allow us to probe the existence of sub–structure in the halos that host the most massive LBGs. A general feature of hierarchical clustering is that more massive halos have higher probability than smaller ones to host more than one galaxy (e.g. Berlind & Weinberg 2002). If the existence of the clustering segregation is due to the fact that LBGs with higher UV luminosity are, on average, more massive than fainter ones, then one prediction is that brighter LBGs should also show a tendency to have more closely associated galaxies than fainter ones. Our deep ACS sample seems well suited to carry out this test, because satellite galaxies are typically less massive than the central galaxy of the halo (Berlind & Weinberg 2002), and because less massive galaxies apparently have fainter UV luminosity. It is likely that pairs, or multiplets, in which one or more members are significantly fainter than the brightest one are under–represented in the shallower ground–based samples. Unfortunately, the lack of systematic redshift measures prevents us from identifying individual physical pairs. Our measure will have to be statistical in character, and signal–to–noise will be lost due to projection.

In our samples, pair statistics on small scales reflect not only large–scale structure of dark matter (via projected close–pairs) but also the physics of galaxy formation within given halos (via physical close–pairs). In this section, we discuss small scale statistics of the ACS selected samples only (B_{435} and V_{606}–band dropouts).

As shown in Figure 2, a significant departure from a power–law on small scales is observed in our $w(\theta)$ measures, most pronounced at the scale of $\theta < 10$ arcsec. 10 arcsec corresponds to roughly 0.3 – 0.4 h^{-1} Mpc comoving at redshift 3 – 5. Recently, Ouchi et al. (2005b) detected a similar small–scale excess in their $w(\theta)$ measurement of $z \sim 4$ galaxies selected from a deep wide–field survey in SXDF field (Ouchi et al. 2004). Steepening on small scales seems to be present in all samples, which we verify by fitting the $w(\theta)$ measurement of each sample to a power–law when the data points with separations $\theta \leq 10$ arcsec are included, in which case we find that the slope is substantially steeper. The slopes of the power–law fits in both cases are shown in Figure 4 for the B_{435} and V_{606}–band dropouts.

This is consistent with the theoretical expectation that there are two separate contributions to $w(\theta)$ or $\xi(r)$, namely a one–halo term and a two–halo term, the origins of which are fundamentally different in nature. The two–halo term reflects the spatial distribution of host dark halos by counting galaxy pairs that belong to two distinct halos. This term dominates large–scale behavior of the correlation function and vanishes on small scales due to the halo exclusion effect, namely two halos cannot coexist closer than their typical size. In contrast, the one–halo term accounts for galaxy pairs sharing the same halo and is dominant on small scales. This reflects how galaxies populate halos. In this context, the single power–

law nature of the correlation function seen in the local universe is somewhat coincidental because it requires a smooth transition between these two terms to result in pure power–law which is possible only for a certain distribution of galaxies therein. Berlind & Weinberg (2002) argued that the contribution of galaxy pairs in massive galaxy clusters is critical for a smooth transition between these two terms. Clusters must be rare at high redshift, hence this steepening should be more prominent. This is also observed in high–resolution N–body simulations. For example, Kravtsov et al. (2004) measured the correlation function of halos above a given mass threshold identified from such simulations at various cosmic epochs. They found that at $z = 0$ the halo correlation function can be fairly well approximated by a power law at all probed scales. However, at higher redshifts, steepening occurs on small scales, at progressively smaller scales with higher redshifts. As a result, power–law fits using the range of scales 0.1 – 8 h^{-1} Mpc give systematically steeper values of β compared with the fits over the range $\sim 0.3 - 8h^{-1}$ Mpc. In fact, Figure 4 shows a similar behavior (in the angular domain) as Figure 12 of Kravtsov et al. (2004).

Although typical halos at high–z must be much less massive than their present–day counterparts (therefore harboring fewer galaxies per halo), halos at high–mass end may host multiple galaxies. This is consistent with the recent discoveries that protoclusters were already forming by redshift of 4 – 6 (e.g. Ouchi et al. 2005a; Miley et al. 2004). To test for this possibility, we have looked for close galaxy pairs that may share host halos. In light of the luminosity segregation, we have split the full sample based on the z_{850}–band magnitude because statistically selecting bright galaxies is equivalent to selecting the sites of the most massive dark halos. Since the spectroscopic information is not available, we count galaxy neighbors around the brightest LBGs as a function of angular separation only.

We split the galaxies in the full ACS sample ($z \sim 4$) into three sub–groups, $z_{850} \leq 24.3$, $m^* < z_{850} \leq 25.0$ and $m^* + 0.5 \leq z_{850} \leq 27.0$ where m^* for the B_{435}–band dropouts is roughly 24.7 (M. Giavalisco et al, in preparation). The number of galaxies in each group is 29, 93 and 2150, respectively. We consider galaxies in the two bright groups as candidates for central galaxies in halos, and the ones in the faintest group as satellite galaxies. We count the number of faint neighbors ($z_{850} \geq m^* + 0.5 \sim 25.2$) around the first two bright groups as a function of angular separation. The upper left panel of Figure 5 shows the average number of neighbors (cumulative counts) around these two bright groups up to 50 arcsec with 1σ Poisson errors, however, these errors should be considered strictly as lower limits because these are correlated. What is expected for an uncorrelated population with the same surface density is also shown with the dashed line. Due to the clustering, both $z_{850} \leq 24.3$ and $24.7 < z_{850} \leq 25.0$ are well above the dashed line, however, $z_{850} \leq 24.3$ galaxies have more neighbors than the other ($\approx 2.5\sigma$). This cannot be understood in terms of the difference in their (large–scale) clustering strength because the same galaxies (therefore with the same

clustering strength) are counted as faint neighbors. In addition, there is clearly no reason to believe that bright galaxies have more galaxies along the line of sight which would be included as projected close–pairs. Another way to confirm that the difference does not come from clustering is to look at the same pair counts on larger scales. The upper right panel of Figure 5 shows the counts at $100 - 160$ arcsec where the two slowly converge. This is because on large scales the contribution from halo–halo clustering dominates the counts thus reflecting the overall clustering strength. To remove the effect coming from the clustering, we take the ratio of the two which is shown in the lower panels. The ratio exceeds unity at $\theta < 30$ arcsec and slowly goes back to unity on larger scales.

This is compelling evidence that we are indeed observing central–satellite galaxy pairs sharing the most massive halos. This is also a natural outcome of the luminosity segregation in that the most massive halos (hosting the brightest LBGs) are likely to have sub–structures massive enough to form satellite galaxies bright enough for us to detect. We have tried a similar neighborhood search for the U–band dropouts, but failed to detect the same trend. Because the U–band dropouts have larger area coverage thus larger number of bright sources, we have increased the magnitude cut for the brightest group up to $R = 22.0$ but still the brightest group does not evidently have more neighbors than the rest. It is possible that the relatively shallow depth of our U–band data plays an important part in the lack of faint neighbors. If, for simplicity, no evolution of the luminosity function is assumed from $z \sim 3$ to $z \sim 4$, one needs U–band dropouts fainter than $R = m^* + 0.5 = 25.0$ ($m^* \sim 24.5$; Adelberger & Steidel 2000) to carry out neighbor counts at a similar luminosity level to the B_{435}–band dropouts case. In other words, we may be seeing only the bright end of the luminosity function where there is essentially one–to–one correspondence between host halos and galaxies. It is consistent with Adelberger et al. (2005)'s data that have comparable depth based on which they concluded that there is little evidence of galaxy multiplicity and that the fraction of dark halos hosting more than one galaxy is about 5%. Another possibility, though minor, is that the relatively poor seeing of our R band, which is where galaxy detection is carried out, prevents detection and deblending of pairs that are closer than 2 arcsec.

6. The Halo Occupation Distribution at $z \sim 4$ and 5

So far we have discussed the measures of the angular correlation function of LBGs, the implied spatial correlation length, and we have reported evidence of a departure of the correlation function from a single power law. We have also shown direct evidence of sub–structure in the most massive halos in the form of number counts of faint LBGs around

the brightest ones on scales $\theta \leq 10$ arcsec. Finally, we have also measured the clustering segregation, namely the fact that brighter LBGs are more strongly clustered in space. In order to understand these results in light of underlying physics, we need to compare with theoretical predictions through which quantitative interpretations of the result can be made.

Associating the spatial distribution of galaxies with that of dark halos requires an understanding of the relationship between galaxy properties and those of host halos, for example, galaxy colors, stellar mass or luminosity are correlated with circular velocity, total mass of halos and so forth. We do not yet know if all the halos above a certain mass threshold host galaxies with similar SEDs (colors) and luminosity to those of LBGs to be included in our sample. At $z \sim 3$, a population of red galaxies, either heavily obscured by dust or old, dubbed as DRGs, which are bright in the near–infrared have been found at similar redshifts with about half the space density of U–band dropouts ($\mathcal{R} \leq 25.5$) (Franx et al. 2003; van Dokkum et al. 2003). Many of these galaxies would not have been selected via the Lyman Break technique. Moreover, the submillimeter galaxies, though their space density is much smaller ($(2.4 \pm 1.2) \times 10^{-6}$ Mpc^{-3}; Chapman et al. 2003), also coexist in the same redshift range. These high–z populations (including LBGs) suffer from respective selection biases thus cannot be solely representative of high–z population in general. The halo occupation distribution (HOD) is a simple model that sets a statistical relationship between halo mass and its probability to form galaxies, thus provides us with a powerful tool to understand the characteristics of different populations independently and study their respective relations to host halos. The HOD formalism has been successfully applied to various local galaxy samples (e.g. different luminosities, colors, spectral types etc.; Zehavi et al. 2004b, Magliocchetti et al. 2003) and also at intermediate redshift (QSOs; Porciani et al. 2004). Note that the HOD formalism can be extended to the conditional luminosity function (CLF; Yang et al. 2003, van den Bosch et al. 2003), to understand the relationship between halo mass and galaxy luminosity. We are currently working to constrain this relationship at $z \sim 3, 4$ and 5 using very large samples of LBGs extracted from the COSMOS 2–square degree survey, which provide excellent sampling at the high end of the luminosity (and hence mass) distribution (K.-S. Lee et al. in preparation).

We move on now to consider a simple model for the halo occupation distribution function, which can be used to understand the phenomenology of the observed clustering properties of LBGs in physical terms, and derive its parameters. These include the minimum mass of halos that can host the observed galaxies and the average halo mass for each galaxy sub–sample. We will then use the best–fit HOD parameters to discuss the inferred halo bias and its implications.

6.1. The HOD Formalism and its Physical Implications

The angular correlation function can be considered to have two separate contributions, galaxy pairs from the same halo and from two distinct halos.

$$w(\theta) = w_{1h}(\theta) + w_{2h}(\theta) \tag{6}$$

On large scales, only $w_{2h}(\theta)$ contributes to the total angular correlation function because any galaxy pair with a large angular separation cannot reside in the same halo. On the other hand, on small scales and on scales comparable to virial diameter of halos, both terms will be present with a ratio that depends on the degree of galaxy multiplicity. The two–halo term can be constrained from clustering measurements; however, the galaxy multiplicity function or halo occupation distribution (HOD) is not very well constrained at high redshifts because of the still relatively small and shallow sample. Bullock et al. (2002) estimated the HOD from a sample of 800 LBGs with spectroscopic redshifts at $z \sim 3$ based on a ground–based survey ($\mathcal{R} \leq 25.5$; Steidel et al. 1998). Although this sample has the advantage of having spectroscopic information, the median luminosity of the sample is significantly brighter than our ACS sample at $z \sim 4$, and thus the number of faint members of pairs or multiplets is very likely quite small. Adelberger et al. (2005) estimate that at most 5% of their LBGs at $z \sim 3$ (an extended version of the sample used by Bullock et al. 2002) are members of close pairs. We do not yet know the luminosity function of satellite LBGs; however, our neighborhood analysis discussed earlier for the B_{435}–band dropout sample at $z \sim 4$ showed that a large fraction of the excess number of neighbors comes from $z_{850}> 26$ (galaxies counted as faint neighbors have $25.2 \leq z_{850} \leq 27.0$). Using our template LBG spectrum, $z_{850}= 26.0$ corresponds to $\mathcal{R} = 25.5$ at $z \sim 3$, that is the limiting flux of Adelberger et al.'s sample. While the bright members of pairs and multiplets are certainly present in their sample, Adelberger et al.'s sample must be highly incomplete for satellite galaxies.

Once the halo power spectrum is given and an HOD model assigned, one can unambiguously determine the correlation function (Seljak 2000; Berlind & Weinberg 2002; Berlind et al. 2003) with suitable assumptions as to how galaxies are distributed within halos (see later). We adopt a simple functional form (Jing et al. 1998; Wechsler et al. 2001). This model assumes that all galaxies are associated with dark matter halos and makes a simplifying assumption that the number of galaxies within a given halo depends only on the halo mass and can be modelled by a single power–law:

$$\begin{aligned} \langle N_g(M) \rangle &= (M/M_1)^{\alpha} \quad if\ M \geq M_{min} \\ &= 0 \qquad\qquad\quad otherwise \end{aligned} \tag{7}$$

where M_1 is the typical halo mass at which there is on average one galaxy per halo, M_{min} is

the cutoff halo mass below which halos cannot host galaxies and α is the power–law index, the efficiency of galaxy formation within halos of given mass M.

While these three parameters, M_1, M_{min} and α are sufficient to constrain the correlation function on large scales, the shape of the correlation function on small scales also depends on how galaxies populate host dark halos. This is because the one–halo term w_{1h} is proportional to $\langle N_g(N_g - 1)\rangle$ while w_{2h} is proportional to $\langle N_g \rangle$ (see Appendix A. for details). Berlind & Weinberg (2002) discussed what these effects are and their impact on the shape of the correlation function on small scales. This includes the scatter of N_g around the mean, galaxy concentration with respect to halo concentration, the existence of a central galaxy at all times and the galaxy velocity dispersion with respect to that of halos. These factors can be used to construct more sophisticated models to constrain the HOD once a larger galaxy sample becomes available. However, at high redshift, the number of galaxies included in any sample (so far) remains much smaller than that in such surveys as 2dF or SDSS, hence a simple approach seems preferable. Therefore we make simplifying assumptions to this model as follows. We force the first galaxy to be placed at the center of host halos and the rest (satellite galaxies) largely follow the halo mass distribution for which we adopt an NFW profile (Navarro, Frenk & White 1997). The latter is consistent with the finding of Kravtsov et al. (2004) that the sub–halos in their simulations follow the distribution of dark matter within the halos.

In order to calculate $w(\theta)$ we closely follow the recipe given by Hamana et al. (2004), using the procedure described in Appendix A. We generate a library of model $w(\theta)$'s for a wide range of (M_1, α) and determine the best–fit $w(\theta)$ that matches the abundance (n_g) and the clustering strength (M_{min}, α and M_1) simultaneously using χ^2 minimization. Note that M_{min} is not a free parameter once the space density is specified.

$$\begin{aligned} n_g(z) &= \int_{M_{min}}^{\infty} n_h(M)\langle N_g(M)\rangle dM \\ \langle n_g \rangle &= \frac{\int dz N(z)[dV(z)/dz] n_g(z)}{\int dz N(z)[dV(z)/dz]} \end{aligned} \tag{8}$$

where $N(z)$ is the redshift selection function obtained from the simulations and $n_h(M)$ is the halo mass function for which we adopt the analytic halo model by Sheth & Tormen (1999, 2002). Note that we derive the HOD parameters, M_1 and α, from the $w(\theta)$ of the full sample (B270 and V270) and do not attempt to constrain these parameters separately for the sub–samples. We also fix the observed number density to the incompleteness–corrected number density integrated down to z_{850}= 27.0 for the fit.

Table 4 lists the HOD parameters obtained using this method for the B_{435} and V_{606}–band dropouts only. For the U–band dropouts, we are unable to put any robust constraints on

these parameters primarily because the HOD fit is most sensitive to $w(\theta)$ at small separations. The $w(\theta)$ measure of the U–band dropouts on such scales seems to indicate a constant value rather than steepening. This is more consistent with the correlation function having the two–halo term only, i.e. each observed galaxy belongs to a different halo, in which case w_{2h} stays relatively constant on small scales ($\xi(r)$ actually falls off but the projection, $w(\theta)$, stays constant due to the contribution from projected galaxy pairs). Figure 6 shows the best–fit model $w(\theta)$ for the full sample of B_{435} and V_{606}–band dropouts with the observational measures. The corresponding confidence levels for the HOD fits are illustrated in Figure 7.

The best–fit parameters for the full samples are (M_{min}, α, M_1) = ($7\times10^{10}h^{-1}M_\odot$, 0.65, $1.3\times10^{12}h^{-1}M_\odot$) for the B_{435}–band dropouts and ($5\times10^{10}h^{-1}M_\odot$, 0.80, $1.0\times10^{12}h^{-1}M_\odot$) for the V_{606}–band dropouts, respectively. Though galaxies were selected with different filter systems and also their sample is shallower, it is interesting to compare them to those of Hamana et al. (2004), ($1.6\times10^{11}h^{-1}M_\odot$, 0.5, $2.4\times10^{12}h^{-1}M_\odot$), ($1.4\times10^{11}h^{-1}M_\odot$, 0.5, $1.4\times10^{12}h^{-1}M_\odot$) for their LBG$z$4s and LBG$z$5s samples. M_{min} is found to be a factor of 2 – 3 smaller from our survey. This is hardly surprising because M_{min} depends mainly on the depth of given survey. Our sample is significantly deeper than theirs ($\approx$ 1 mag) and, because LBGs have compact morphology, more complete in the magnitude range where there is overlap. As a result, the overall clustering strength of our sample is weaker which is most directly reflected in M_{min}. The parameter M_1, the mass scale at which statistically there is one galaxy corresponding to each halo, is smaller in our case, consistent with our expectations. On the other hand, this work and previous studies consistently show that α should be 0.5 –1 though it may be dependent on M (thus the depth). Therefore over a reasonable range of observable halo mass it can be approximated (to the zeroth order) as a constant, thus nearly independent of mass scale. Unfortunately, as can be seen in Figure 7, it is the least constrained parameter from the HOD fit. In principle, however, α can be constrained independently via studies such as our neighborhood analysis or gravitational lensing surveys.

We calculate $\langle N_g\rangle_M$ (note the subscript "M" to distinguish the quantity from the previously mentioned $\langle N_g(M)\rangle$), the ratio of galaxy number density to halo number density ($=n_g/n_h$) integrated over the allowed range of halo mass. We also calculate $\langle M\rangle$, the average mass of halos that host the observed LBGs (assuming the best– fit HOD parameters) as follows:

$$\begin{aligned} \langle N_g\rangle_M &= \frac{\int_{M_{min}}^{\infty} n_h(M)\langle N_g(M)\rangle dM}{\int_{M_{min}}^{\infty} n_h(M)dM} \\ \langle M\rangle &= \frac{\int_{M_{min}}^{\infty} M\langle N_g(M)\rangle n_h(M)dM}{\int_{M_{min}}^{\infty}\langle N_g(M)\rangle n_h(M)dM} \end{aligned} \tag{9}$$

For each sub–sample, we compute M_{min} that matches the number density, then $\langle N_g \rangle_M$ and $\langle M \rangle$ are computed using the best–fit HOD parameters. Table 4 summarizes the results. Uncertainties are computed by propagating the bootstrap errors of $w(\theta)$ after marginalizing over M_1 and α. We find $\langle N_g \rangle_M = 0.3$ and 0.2 for the full sample of B_{435}–band and V_{606}–band dropouts, respectively. If each galaxy belongs to a different halo, this quantity would represent the average number of galaxies per halo. For example, for our B_{435}–band dropouts, this means that only 30% of the halos harbor LBGs bright enough to be detected (in other words, 30% of the halos that are more massive than M_{min}). In reality, where multiple galaxies can share host halos, $\langle N_g \rangle_M$ can be regarded as an upper limit. Note that Adelberger et al. (2005) and Giavalisco & Dickinson (2001), based on the ground–based sample with $\mathcal{R} \leq 25.5$, argued that most halos at $z \sim 3$ host visible LBGs. While it is not clear if their claim is in quantitative discrepancy with our estimate, we note that possible evolutionary effects from $z \sim 4$ to $z \sim 3$ remain poorly understood at this time. It is interesting, however, that the B_{435}–band dropouts with $z_{850} \leq 26.0$ (B260), which have a comparable absolute luminosity threshold to that of the U–band dropouts of $\mathcal{R} \leq 25.5$ (U255), have $\langle N_g \rangle_M \sim 0.5$, similar to what Adelberger et al. (2005) have found (see their Figure 10). This suggests that LBGs at $z \sim 3$ and 4 of similar luminosity also have a similar duration of star–formation during which they are visible (duty–cycle hereafter). Note that if the average galaxy luminosity is closely tied to the halo mass, as suggested by the clustering segregation, then in principle one can empirically find the intrinsic relationship between UV luminosity and mass at a given redshift[2]. For example, given a mass spectrum and a HOD function, such a relationship will simulataneously reproduce the shape of the correlation function, that of the clustering segregation, and the luminosity function. Interestingly, when the same absolute magnitude cut is made to the V_{606}–band dropouts, we find that $\langle N_g \rangle_M$ is a factor of 2 – 3 smaller. We postpone the interpretations of these results to the next subsection. Finally, we note explicitly that the clustering properties of LBGs are consistent with the notion, built in the HOD model itself, that $\langle N_g \rangle_M$ becomes smaller for less massive halos. A possible physical explanation for this fact could be that in low–mass halos, gas cooling (hence star formation) is much more inefficient due to photo–ionization (squelching) or SNe feedback (e.g. Silk 1997, Efstathiou 2000). In addition, it is possible that the duty–cycle of galaxies may be mass–dependent such that lower–mass halos have shorter duty–cycle, thus resulting in a smaller value of $\langle N_g \rangle_M$.

---

[2]This would be the average "observed" UV luminosity, not corrected for the effects of dust obscuration. Since not all galaxies have the same dust obscuration, and since the amount of dust obscuration is, in general, dependent on the UV luminosity itself, the statistical relationship between obscured and unobscured UV luminosity and mass will be, in general, different.

6.2. A Different Approach: Separation of Central and Satellite Galaxies

We have also explored an alternative approach, which is to model central galaxies and satellites separately (Guzik & Seljak 2002; Kravtsov et al. 2004; Zheng et al. 2005) In this model, the probability for a halo to have a central galaxy is a step function, namely either the halo has a central galaxy or it does not, whereas the distribution of satellite galaxies follows a power–law:

$$\begin{aligned} \langle N_g(M) \rangle &= 1 + (M/M_1')^{\alpha'} \quad if\ M \geq M_{min}' \\ &= 0 \qquad\qquad\qquad\quad otherwise \end{aligned} \tag{10}$$

We refer to this model as the "one–plus" model as opposed to the previous one which we refer to as the "pure power–law" model hereafter. Note that the normalization M_1' and the threshold mass M_{min}' have different physical meanings in this model compared to the previous one. In the present model the parameter M_1' is the halo mass at which there is one satellite galaxy (thus two galaxies in total) in the host halo. The parameter M_{min}' is conceptually the same as M_{min} of the first model, except that now halos above this threshold value always have $\langle N_g \rangle \geq 1$, while in the pure power–law model only a fraction of halos with $M > M_1$ are host to more than one galaxy on average. Using the alternative model for the halo distribution function of Lyman–break galaxies we find that the best–fit parameters for the B_{435}–band dropouts are $(M_{min}', \alpha', M_1') = (2 \times 10^{11} h^{-1} M_\odot, 1.3, 4 \times 10^{12} h^{-1} M_\odot)$.

We have fit the two HOD models to our data, and the χ^2 analysis shows that both reproduce the observed $w(\theta)$ equally well. Figure 8 shows the predicted $w(\theta)$ from the best–fit HOD parameters in both cases together with the observed correlation function of the B_{435}–band dropouts. We found $\chi^2_{1+} = 0.97$ and $\chi^2_{ppl} = 0.91$. In addition, they predict similar $\langle N_g \rangle$ for mass scales of $10^{12} - 10^{13}\ h^{-1} M_\odot$, to which most of massive halos included in the sample belong. This is shown in the right panel of Figure 8. At the high–mass end ($M > 10^{13} h^{-1} M_\odot$), however, the two models diverge from each other rather quickly. To constrain the HOD function in this mass range one needs a much larger sample covering significantly more area than the GOODS, because of the rarity of high–mass halos. On scales $M < 10^{12} h^{-1} M_\odot$, on the other hand, the "pure power–law" model predicts numerous low–mass halos being included in the sample with a relatively low efficiency of actually hosting a galaxy, while for the "one–plus" model, $\langle N_g \rangle$ is truncated (by definition) at the mass scale of $M < 2 \times 10^{11} h^{-1} M_\odot$.

Finally, we observe that although the two models are equally good at reproducing the observations, this is very likely the result of the still relatively large uncertainties in the measure of $w(\theta)$. The rationale behind the "one–plus" model is that every single halo above M_{min} participates in forming observed galaxies. In contrast, the "pure power–law" model

allows a fraction of halos to form galaxies over some range of mass ($M < M_1$), with the complementary fraction remaining quiscent (either because no star formation has not started in them or becuase observed in between bursts of star formation). The currently available data at high rdshifts do not allow us to test which model is a better representation of reality. However, we note that the built–in assumption of the "one–plus" model, that there is always one central galaxy (in our case, one LBG), in every halo above a mass threshold, naturally precludes the possibility of having other types of galaxies (i.e. non–LBG) as the central galaxy in those halos. While such a limitation is not a problem in the local universe, it is very likely a misrepresentation of the situation in the high–redshift universe. For example, a number of observations have shown the existence of massive galaxies at $z \sim 3$ whose UV spectral energy distribution is such that they would not be selected as Lyman-break galaxies. Such galaxies very likely have masses that are in the high–mass end of the LBG mass range (e.g. Shapley et al. 2004, van Dokkum et al. 2004). The "one–plus" model would not provide a fair representation of the HOD if such galaxies are relatively common at high redshift. For these reasons we will limit the discussion only to the "pure power–law" model in what follows.

Realistically, we expect observed LBGs to be the central galaxies in only a certain fraction of halos ($M \geq M_1$). For this reason, we expect that $\langle N_g \rangle = p + (M/M_1)^\alpha$ ($M > M_{min}$ with $0 < p < 1$) may be a more reasonable description of the actual halo occupation distribution such that a fraction $1 - p$ is reserved for other populations. While M_1 and α (to a lesser extent) may depend on the depth of a given survey, p more likely represents a fundamental quantity that is the efficiency of LBGs as central galaxies on the high end of the halo mass function. We plan to explore this possibility in a follow–up paper with a larger data set (K.-S. Lee et al., in preparation).

6.3. The Evolution of Halo Bias with Redshift

We compute the nonlinear autocorrelation function of matter ξ_m(r) at redshift $z \sim 3$, 4 and 5 by adopting the algorithm by Peacock & Dodds (1996). ξ_m(r) is then inverted to $w_m(\theta)$ using the Limber transform as follows:

$$w_m(\theta) = \frac{\int_0^\infty dz N^2(z) \int_{-\infty}^\infty [dx/R_H(z)] \xi_m([D_M(z)\theta]^2 + x^2)^{1/2}}{[\int dz N(z)]^2} \tag{11}$$

where $D_M(z)$ is the proper motion distance and $R_H(z)$ the Hubble radius at given redshift z. Using this method, the average bias is calculated as a function of angular separations.

$$\langle b_{obs}(\theta)\rangle = \sqrt{\frac{w(\theta)}{w_m(\theta)}} \tag{12}$$

The bias $\langle b_{obs}(\theta)\rangle$ monotonically decreases at small separations then stays constant at $\theta \geq 70$ arcsec. We adopt the value of $\langle b_{obs}\rangle$ at 100 arcsec as our linear bias value. The theoretical predictions of the galaxy and halo bias can be computed from the given halo model as follows:

$$\begin{aligned} \langle b_g\rangle &= \frac{1}{n_g}\int_{M_{min}}^{\infty} n_h(M) b_h(M)\langle N_g(M)\rangle dM \\ \langle b_h\rangle &= \frac{1}{n_h}\int_{M_{min}}^{\infty} n_h(M) b_h(M) dM \end{aligned} \tag{13}$$

where $n_h = \int_{M_{min}}^{\infty} n_h(M)dM$ and $n_g = \int_{M_{min}}^{\infty} n_h(M)\langle N_g(M)\rangle dM$. We use the best–fit HOD parameters for $\langle N_g(M)\rangle$. Note that halo bias $\langle b_h\rangle$ is HOD–independent whereas $\langle b_g\rangle$ is not. The observed galaxy number density is calculated by fitting the full sample to the Schechter luminosity function after correcting for photometric incompleteness (e.g. Giavalisco 2005) and integrating down to each magnitude cut (see Table 3). The error bars in the number density are derived by propagating the uncertainties from the Schechter LF fit.

Figure 9 shows the average galaxy bias from the clustering measures together with the predictions of $\langle b_h\rangle$ and $\langle b_g\rangle$ at $z \sim 4$ and 5. Note that the abscissa represents the halo abundance (n_h) for the dashed lines and the galaxy abundance (n_g) for the solid lines and symbols ($n_g = n_h$ if $N_g \equiv 1$). The observed galaxy bias values are in good agreement with the CDM model predictions when the best–fit HOD parameters are assumed.

To compare the results from different cosmic epochs, it is important to remove the effect of the luminosity segregation which could be mistakenly interpreted as "evolution". We truncate each sample to the same absolute luminosity threshold to match that of our brightest sample, the U–band dropouts ($R \leq 25.5$), the absolute magnitude of which is $M_{1700} \leq$ -20.0. This corresponds to $R \leq 25.5$, $z_{850} \leq 26.0$ and $z_{850} \leq 26.6$ at $z \sim 3$, 4 and 5, respectively. Since these luminosity thresholds are similar to those of the U255, B260 and V265 sample, we compare the bias values for these magnitude cuts. Figure 10 illustrates how these bias values change with redshift compared to halo biases for various mass thresholds. The dashed lines indicate the evolution of the average halo bias with a constant halo mass threshold for $M_{halo} = 10^{10}, 5\times10^{10}, 10^{11}, 5\times10^{11}, 10^{12}$ and $5\times10^{12}\ h^{-1}M_\odot$ (from bottom) from the Sheth & Tormen (1999) model. Lines serve as as a guide to determine the effective halo mass threshold of a given galaxy sample.

It is intriguing that our measures at $z \sim 3$ and 4 imply that these galaxies are hosted by

halos of mass $5 \times 10^{11} h^{-1} M_\odot \lesssim M_{halo} \lesssim 10^{12} h^{-1} M_\odot$, however, at $z \sim 5$, the host halo mass is approximately $10^{11} h^{-1} M_\odot$, a factor of $5 - 10$ times smaller than its lower–z counterparts at a given fixed luminosity. Hamana et al. (2004) reported the average bias of their LBGz4s with similar absolute luminosity threshold, $i' \leq 26.0$, to be 3 – 4.5, consistent with our results. This implies that at $z \sim 5$, star–formation may have been more efficient, hence galaxies of comparable luminosities were hosted in much lower–mass halos. This result is, in fact, another manifestation of what we have mentioned in an earlier subsection, that $\langle N_g \rangle$ was a factor of 2 – 3 smaller at higher redshift when the same absolute luminosity cut was made for a given choice of HOD parameters.

7. Summary

1. We have studied the spatial clustering properties of LBGs at three different cosmic epochs. We used three samples of LBGs which include two deep ACS–selected LBGs samples at $z \sim 4$ and 5 down to a magnitude limit of $z_{850} \sim 27$ and the ground–based sample at $z \sim 3$ down to $R \sim 25.5$. The ACS samples enable us to study the spatial distribution of the large–scale structure as well as of small–scale clustering whereas the ground–based sample allows us to probe the large–scale clustering of bright LBGs selected from a large contiguous area.

2. We found that the clustering strength (the amplitude of $w(\theta)$ or value of r_0) of LBGs at all redshifts that we have studied depends on the UV luminosity (rest–frame $\lambda \approx 1700$ Å) of the galaxies. This luminosity segregation is in good quantitative agreement with previous investigations based on much brighter galaxy samples and we are able to robustly extend this reesult down to at least 1 mag fainter than previous studies. The faintest galaxy sub–sample has a real–space correlation length as small as 2 h^{-1} Mpc, only half of that known for $\mathcal{R} \leq 25.5$ sample. A physical implication is that galaxies brighter at UV wavelengths are hosted by more massive dark halos, implying that the star–formation is primarily regulated by local gravity, and suggesting that other physical mechanisms (major mergers, interactions) are secondary drivers.

3. We have carried out neighbor counts around bright LBGs in our sample and counted the number of bright–faint galaxy pairs. We discovered that the likelihood of finding faint neighbor galaxies ($z_{850} \gtrsim m^* + 0.5$) around bright ones ($z_{850} \leq 24.3$) up to scales comparable to the virial radius of dark halos, is at least $20 - 30$ % higher than random LBG–LBG pairs with a high significance. This is consistent with the interpretation that there are faint companions around the brightest galaxies sharing host halos, supporting that the departure of the correlation function on small scales (from the extrapolation of the large–scale power–law) is

indeed due to central–satellite pairs. The observed sub–structure is also consistent with the luminosity segregation that we have detected, in that brighter galaxies (more massive halos) are likely to have fainter companions (halo sub–structures). We do not yet know the relationship between the UV luminosity and the actual host halo mass. However, the clustering segregation gives support to the interpretation that the most luminous LBGs are hosted by the most massive halos and tend to have more satellite galaxies in halo sub–structures. Due to the relatively small dynamic range in magnitude of our survey, we are limited to a bright cut of z_{850}= 26.0 and also to cumulative magnitude thresholds for our samples, however, we expect this effect to be more dramatic in future surveys that cover larger cosmic volume, which should confirm our results.

4. Our measurement of the correlation function at $z \sim 4$ and 5 indicates a steepening on small scales, thus cannot be well described by a simple power–law. We also find that the scale at which the steepening occurs is comparable to the angular size of dark halos at the relevant redshift range, and hence we attribute this steepening to the presence of multiple galaxies within the same halo. A simple HOD model with a suitable scaling law between halo mass and the number of galaxies seems to be able to explain both the large–scale and small–scale behavior of the angular correlation function. We find the best–fit HOD parameters for LBGs at $z \sim 4$ and 5 to be (M_{min} , α, M_1) = ($7 \times 10^{10} h^{-1} M_\odot$, 0.65, $1.3 \times 10^{12} h^{-1} M_\odot$) and ($5 \times 10^{10} h^{-1} M_\odot$, 0.8, $1.0 \times 10^{12} h^{-1} M_\odot$), respectively. With these parameters, we find that, on average, the number density of galaxies is a factor of 4 – 5 smaller than that of dark halos for the full sample and that this discrepancy is smaller for brighter galaxy samples. This suggests that the duty–cycle of faint LBG populations may be shorter than that of brighter counterparts suggested by shallower surveys, but at the same absolute luminosity cut, our results are in good agreement with shallower surveys. However, at $z \sim 3$, our results do not indicate a similar steepening, but is more consistent with a constant value for the correlation function at small scales. We interpret this discrepancy to be caused by the difference in survey depth, as shallower surveys tend to pick up only bright LBGs which probably tend to be central galaxies and not satellites (which are usually fainter) within halo sub–structures that largely produce this small–scale feature.

5. The scaling of the correlation length or galaxy bias as a function of volume density shows a similar trend to that expected for dark halos, implying that our measures fully support the biased galaxy formation scenario predicted by the cold dark matter framework. This suggests that LBGs flag the sites of dark halos efficiently, however, not every halo is lit up at the same time. This has to do with the fact that the duty–cycle of LBGs is shorter than the cosmic time spanned by the observations (0.3 – 0.5 Gyr), therefore only a fraction of halos are lit up by star–formation at any given time. In addition, a HOD that scales with halo mass might be an indication that duty–cycle is also mass–dependent such that

higher–mass halos may have longer duty–cycles than their lower–mass counterparts.

6. We truncate each sample to a fixed absolute magnitude and compute the average bias of these galaxies. At $z \sim 5$, galaxies with a given luminosity are hosted by halos of mass $\sim 10^{11}h^{-1}M_{\odot}$ whereas at $z \sim 3$ and $z \sim 4$, the corresponding host halos are a factor of 5 – 10 more massive. The implication is that at $z \sim 5$ star–formation was more efficient than the later epochs.

We thank Cristiano Porciani for very helpful assistance. KL acknowledges Takashi Hamana for kindly providing his halo code for model comparisons. MG and KL thank David Weinberg for his very useful comments on HOD modelling. We would also like to thank an anynymous referee for useful suggestions. We are grateful to the entire GOODS team and particularly, Tomas Dahlen, who has put great efforts into calibrating many of the GOODS ground–based data sets, which made our ground–based measures possible.

A. $w(\theta)$ and Halo Occupation Distribution

For a given set of (M_1, α) with a fixed number density $\langle n_g \rangle$, the minimum mass M_{min} is determined by matching the number density of the observed galaxies $\langle n_g \rangle$ with that expected from the halo model as follows:

$$n_g(z) = \int_{M_{min}}^{\infty} dM n_h(M) \langle N_g(M) \rangle \tag{A1}$$

$$\langle n_g \rangle = \frac{\int dz N(z)[dV/dz] n_g(z)}{\int dz N(z)[dV/dz]} \tag{A2}$$

where $N(z)$ is the normalized redshift selection function and dV/dz is the comoving volume element per unit solid angle. The contributions from the one–halo and two–halo components are computed from their respective galaxy power spectra, $P_g^{1h}(k, z)$ and $P_g^{2h}(k, z)$. $w(\theta)$ is the inverse Fourier transform of the total power spectrum, $P_g(k, z)$:

$$w(\theta) = \int dz N(z)^2 (\frac{dr}{dz})^{-1} \int dk \frac{k}{2\pi} P_g(k, z) J_0(r(z)\theta k) \tag{A3}$$

where J_0 is the Bessel function of the first kind and $r(z)$ is the radial comoving distance. The one–halo contribution to the power spectrum is given as:

$$P_g^{1h}(k, z) = \frac{1}{n_g(z)^2} \int dM \frac{dn_h}{dM} \langle N_g(N_g - 1) \rangle |y(k, M)|^p \tag{A4}$$

where y is the normalized Fourier transform of the halo mass profile (Seljak 2000; Scherrer & Bertschinger 1991). We further assume that each halo has an NFW profile with the concentration parameter varying with the halo mass as found by Bullock et al. (2001). The parameter p is taken to be $p = 1$ if $\langle N_g(N_g - 1)\rangle < 1$, and $p = 2$ otherwise (Seljak 2000).

The two–halo term contribution to the galaxy power spectrum according to the linear halo bias model (Cole & Kaiser 1989; Mo & White 1996) is:

$$P_g^{2h}(k,z) = P_{lin}(k)\{\frac{1}{n_g(z)}\int dM \frac{dn_h}{dM}\langle N_g(M)\rangle b(M) y(k,M)\}^2 \tag{A5}$$

where $P_{lin}(k)$ is the linear dark matter power spectrum and $b(M)$ is the linear halo bias from the fitting function of Sheth & Tormen (1999).

REFERENCES

Adelberger, K. et al. 1998, ApJ, 505, 18

Adelberger, K. & Steidel, C. 2000, ApJ, 544, 218

Adelberger, K. et al. 2005, ApJ, 619, 697

Allen, P. D. et al. 2005, MNRAS, 360, 1244

Bagla, J. S. 1998, MNRAS, 297, 251

Benoist, C. et al. 1996, ApJ, 472, 452

Berlind, A. A. & Weinberg, D. H. 2002, ApJ, 575, 587

Berlind, A. A. et al. 2003, ApJ, 593, 1

Bertin, E. & Arnouts, S. 1996, A&AS, 117, 393

Bullock, J. et al. 2001, MNRAS, 321, 559

Bullock, J. et al. 2002, MNRAS, 329, 246

Chapman, S. et al. 2003, Nature, 422, 695

Cole, S. & Kaiser, N. 1989, MNRAS, 237, 1127

Daddi, E. et al. 2003, ApJ, 588, 50

Dickinson, M. E. et al. 2004, ApJ, 600, L99

van Dokkum, P. et al. 2003, ApJ, 587, 83

Efstathiou, G. 2000, MNRAS, 317, 697

Ferguson, H. et al. 2004, ApJ, 600, L107

Foucaud, S. et al. 2003 A&A, 409, 835

Franx, M. et al. 2003, ApJ, 587, L70

Giavalisco, M. et al. 1998, ApJ, 503, 543

Giavalisco, M. 2002, ARA&A, 40, 579

Giavalisco, M. & Dickinson, M. E. 2001, ApJ, 550, 177

Giavalisco, M. et al. 2004a, ApJ, 600, L93

Giavalisco, M. et al. 2004b, ApJ, 600, L103

Giavalisco, M. 2005, *proceedings from Wide–Field Imaging from Space* eds. Tim McKay, Andy Fruchter, and Eric Linder

M. Giavalisco et al., in preparation

Gunn, J. E. & Oke, J. B. 1975, ApJ, 195, 225

Guzik, J. & Seljak, U. 2002, MNRAS, 335, 311

Hamana, T. et al. 2004, MNRAS, 347, 813

Jing, Y. P., Mo, H. J. and Boerner, G. 1998, ApJ, 494, 1

Kravtsov, A. et al. 2004, ApJ, 609, 35

Landy, S. & Szalay, A. 1993, ApJ, 412, 64

K.-S. Lee et al., in preparation

Ling, E. N., Barrow, J. D. & Frenk, C. S. 1986, MNRAS, 223, 21

Madau, P. et al. 1995, ApJ, 441, 18

Madau, P. et al. 1996, MNRAS, 283, 1388

Magliocchetti, M. et al. 2003, MNRAS, 346, 186

Miley, G. et al. 2004, Nature, 427, 47

Mo, H. J., & White, S. D. M. 1996, MNRAS, 282, 347

Navarro, J. F., Frenk, C. S. & White, S. D. M. 1997, ApJ, 462, 563

Norberg, P. et al. 2001, MNRAS, 328, 64

Ouchi, M. et al. 2004, ApJ, 611, 685

Ouchi, M. et al. 2005a, ApJ, 620, L1

Ouchi, M. et al. 2005b, submitted to ApJ

Peacock, J. A. & Dodds, S. J. 1996, MNRAS, 280, 19

Peebles, P. J. E. 1980, The Large–Scale Structure of the Universe (Princeton Univ. Press)

Porciani, C. & Giavalisco, M. 2002, ApJ, 565, 24

Porciani, C. et al. 2004, MNRAS, 355, 1010 Recipes (Cambridge: Cambridge Univ. Press)

Riess, A. et al. 2004, ApJ, 600, L163

Roche, N. & Eales, S. 1999, MNRAS, 307, 703

Sheth, R. K. & Tormen, G. 1999, MNRAS, 308, 119

Sheth, R. K. & Tormen, G. 2002, MNRAS, 329, 61

Scherrer, R. J. & Bertschinger, E. 1991, ApJ, 381, 349

Seljak, U. 2000, MNRAS, 318, 203

Shapley, A. E. et al. 2004, ApJ, 612, 108

Silk, J. 1997, MNRAS, 481, 703

Somerville, R. et al. 2004, ApJ, 600, L171

Steidel, C. C. et al. 1995, AJ, 110, 2519

Steidel, C. et al. 1998, ApJ, 492, 428

Steidel, C. et al. 1999, ApJ, 519, 1

Steidel, C. C. & Hamilton, D. 1993, ApJ, 105, 2017

Steidel, C. C. et al. 2003, ApJ, 592, 728

van den Bosch, F. C., Yang, X., Mo, H. J. 2003, MNRAS, 340, 771

Vanzella, E. et al. 2005, A&A, 434, 53

E. Vanzella et al., in preparation

Wechsler, R. et al. 2001, ApJ, 554, 85

White, S. D. M. & Reese, M. 1978, MNRAS, 183, 341

Yang, X., Mo, H. J., van den Bosch, F. C. 2003, MNRAS, 339, 1057

Zehavi, I. et al. 2002, ApJ, 571, 172

Zehavi, I. et al. 2004a, ApJ, 608, 16

Zehavi, I. et al. 2004b, astro-ph/0408569

Zheng, Z. et al. 2005, ApJ, 633, 791

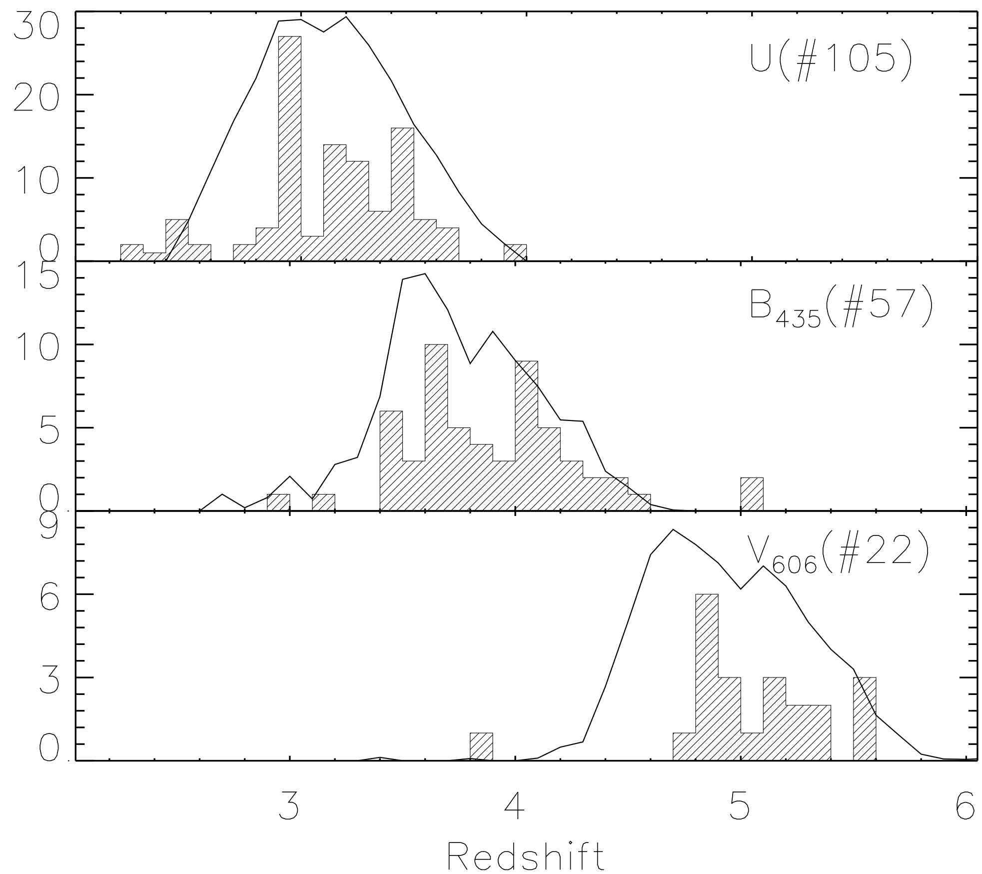

Fig. 1.— The redshift distribution functions $N(z)$ of the U, B_{435} and V_{606}–band dropouts (from top) estimated from Monte Carlo simulations. The coarser histograms indicate the distribution of spectroscopically confirmed objects to date whose numbers are specified on top right corner of each panel. The histograms from the simulations are arbitrarily normalized to match the distribution of the spectroscopic samples.

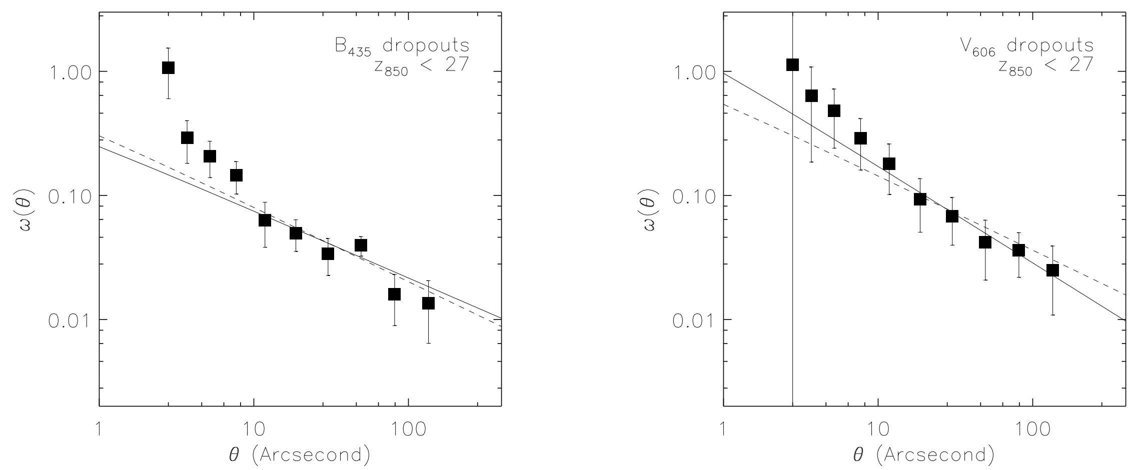

Fig. 2.— The angular correlation function $w(\theta)$ of the B_{435} (the left panel) and V_{606}–band dropouts (the right panel). The points are the measurements corrected for the integral constraint (IC) together with the best–fit power–laws. The solid line shows the results when the slope is allowed to vary and the dashed line shows the result when the slope is fixed to 0.6. The fit is done including angular separations $\theta > 10$ arcsec only. While the data can be well described by a single power–law on large scales, a significant departure from a power–law on scales $\theta < 10$ arcsec is observed.

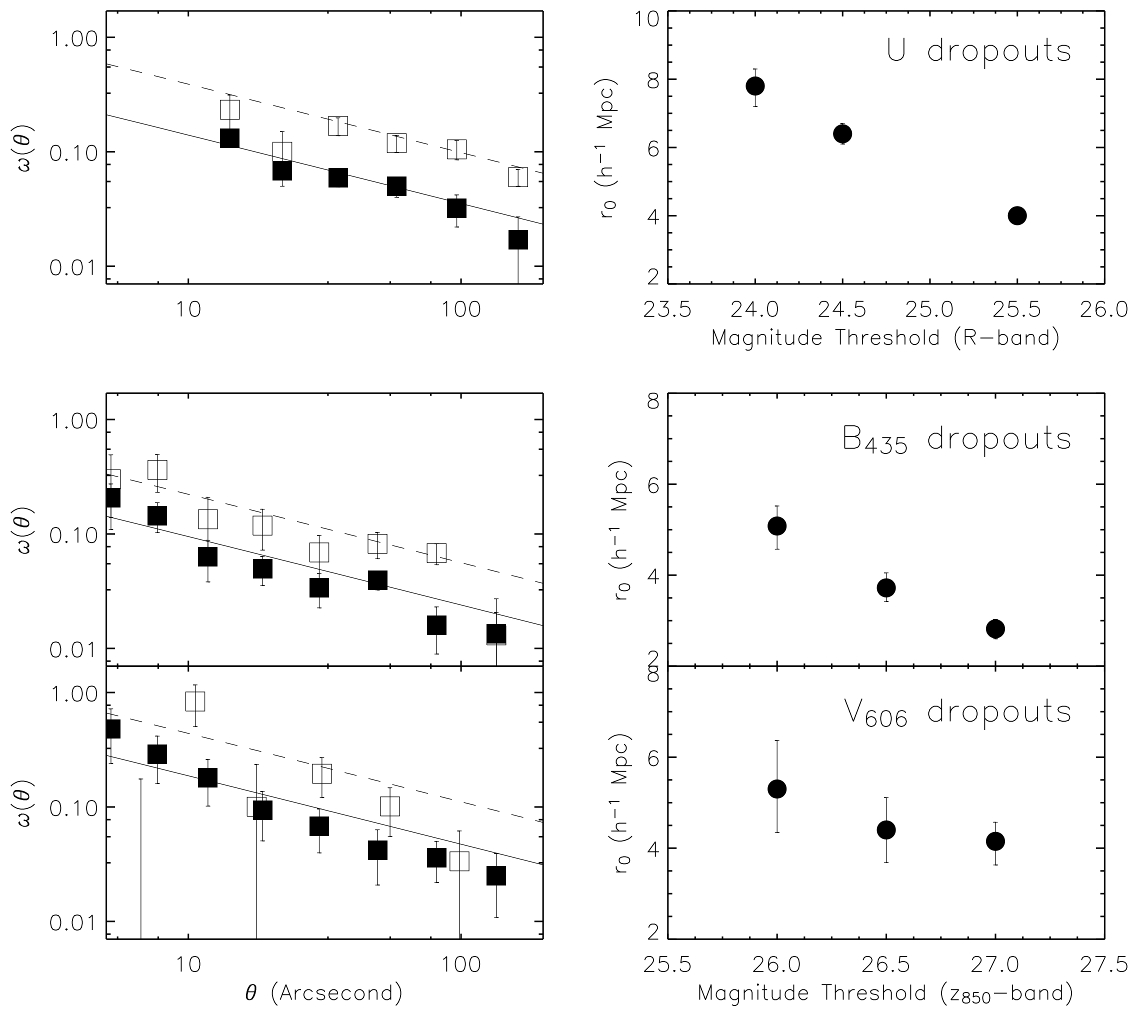

Fig. 3.— Left panels: The angular correlation function $w(\theta)$ of the U, B_{435}, V_{606}–band dropouts (from top). The filled symbols show the measures from the full sample (ACS–based: $z_{850} \leq 27.0$, ground–based: $R \leq 25.5$) while the open symbols show results from the brightest sub–sample (ACS: $z_{850} \leq 26.0$, ground–based: $R \leq 24.0$) together with the best–fit power–law when the slope is forced to be $\beta = 0.6$. The correlation amplitude, A_w, increases by a factor of more than 2 for the brighter groups in each case. Right panels: The real–space correlation length r_0 is shown as a function of the magnitude thresholds used to define each sample. Note that the top–right panel is R–based ($R \leq 24.0$, 24.5 and 25.5), whereas the others are z_{850}–based ($z_{850} \leq 26.0$, 26.5 and 27.0).

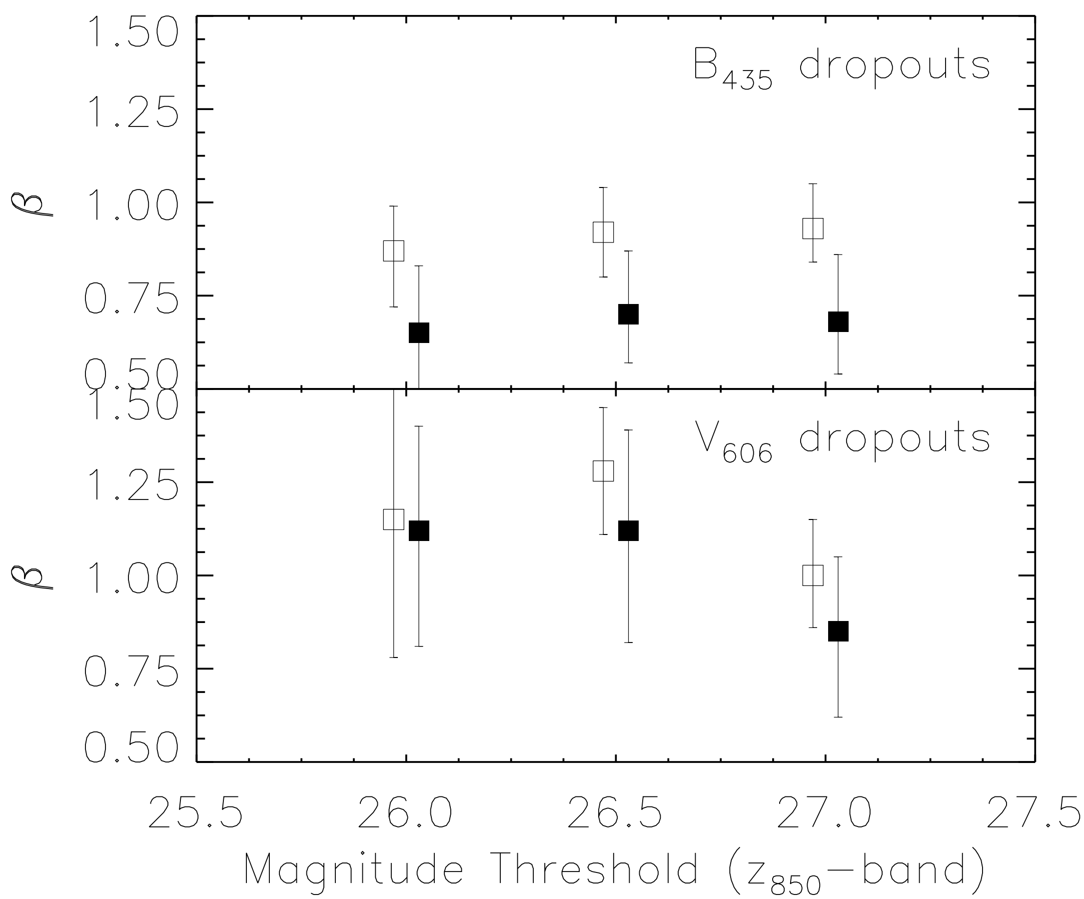

Fig. 4.— The steepening of the correlation slope on small scales: both panels show the best–fit slope of the correlation function for samples with a given apparent magnitude threshold. The filled (open) symbols show the slope β when fitted to a single power–law without (with) the observational measures at angular separations of $\theta < 10$ arcsec. This is due to an excess number of physically close galaxy–pairs causing a significant departure from a pure power–law at small separations.

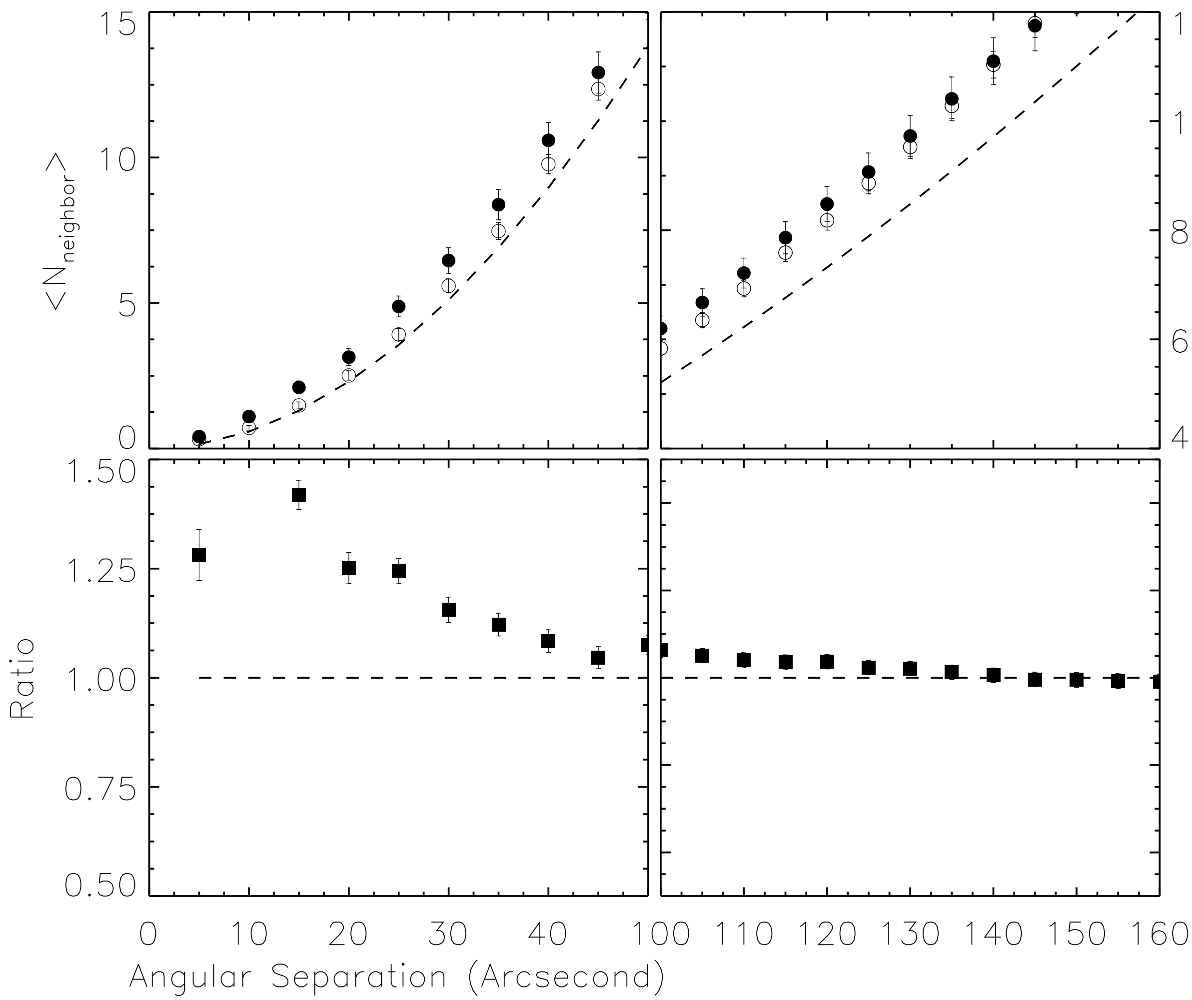

Fig. 5.— The top panels show the average number of faint LBG neighbors ($z_{850} \geq m^* + 0.5$; $m^* = 24.7$ at $z \sim 4$) as a function of angular separation around the two bright groups, $z_{850} < 24.3$ (filled) and $m^* \leq z_{850} \leq 25.0$ (open), together with what is expected for purely random distributions ($w = 0$), shown as the dashed lines. The error bars represent Poisson errors. The bottom panels show the ratio of the two quantities shown in the top panels. Taking the ratio of the two essentially removes the effect from the projected galaxy pairs, providing a better indication of the true excess due to physical pairs. The galaxies that belong to the brightest group ($z_{850} < 24.3$), on average, have more faint LBG neighbors (3σ significance) than the other group ($m^* \leq z_{850} \leq 25.0$). This effect is most pronounced at $0 < \theta < 30$ arcsec. The ratio slowly drops down to unity on larger scales. This is consistent with the halo sub–structure interpretation because when the angular separation is comparable to the typical distance between nearby halos, $\langle N_{neighbor} \rangle$ is dominated by large–scale clustering rather than halo sub–structure.

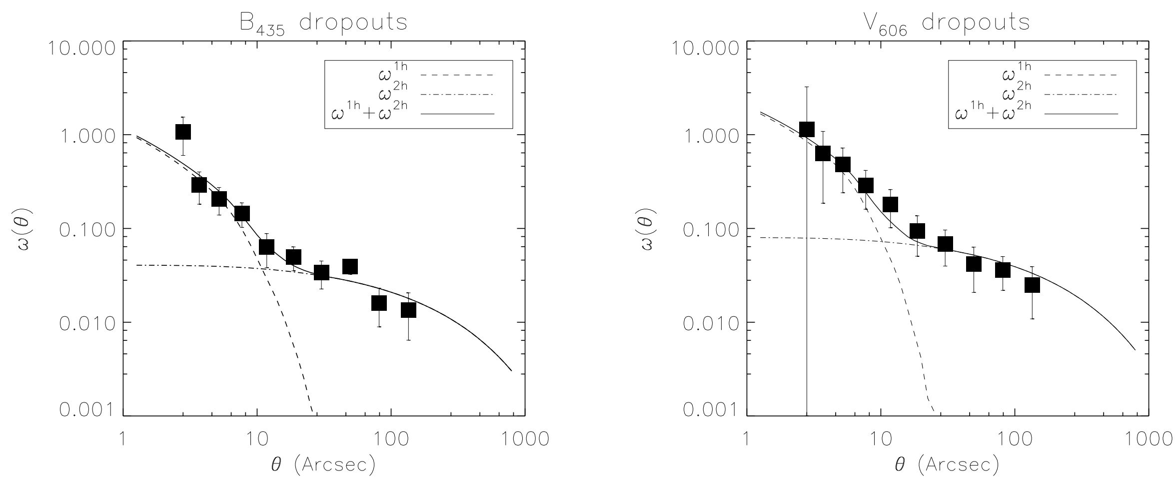

Fig. 6.— The two–component fit with the best–fit HOD parameters is shown together with the observed angular correlation function. The dashed line shows the one–halo contribution and the dashed–dot line shows the two–halo contribution to the final $w(\theta)$. The solid line is the sum of the two contributions. The best–fit HOD parameters are $M_{min} = 7 \times 10^{10} h^{-1} M_{\odot}$, $M_1 = 1.3 \times 10^{12} h^{-1} M_{\odot}$ and $\alpha = 0.65$. Right: the V_{606}–band dropouts: The best–fit HOD parameters are $M_{min} = 5 \times 10^{10} h^{-1} M_{\odot}$, $M_1 = 1.0 \times 10^{12} h^{-1} M_{\odot}$ and $\alpha = 0.80$.

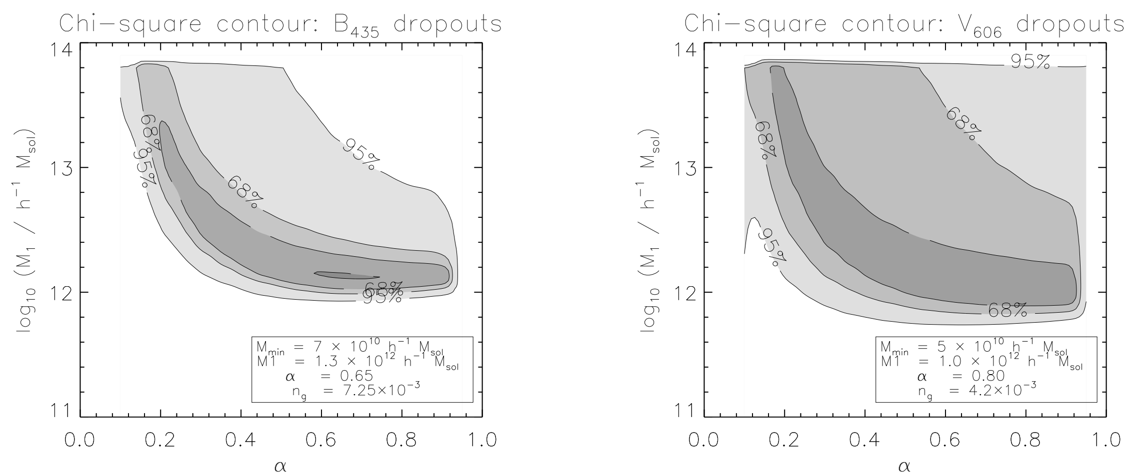

Fig. 7.— The χ^2 contour map of the HOD fits overlaid with confidence intervals for the B_{435} (left) and V_{606}–band (right) dropouts: M_1 vs. α. The contour lines show $\Delta\chi^2 = 2.3$ and 6.2, corresponding to 68% and 95% confidence levels. Boxes on the bottom right corners show the best–fit HOD parameter values and the galaxy number density.

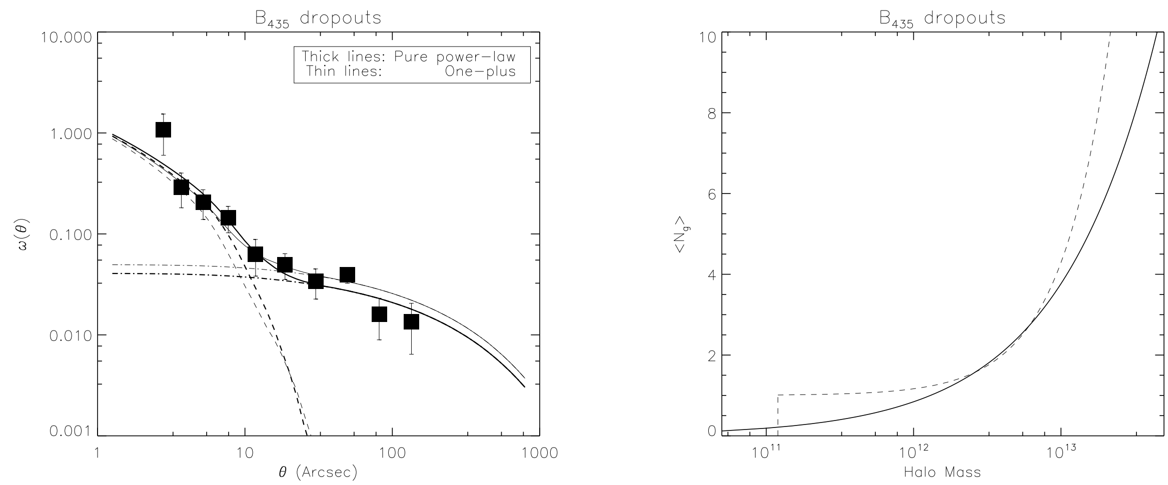

Fig. 8.— Left panel: The two–component fit of the "pure power–law" (thick lines) and "one–plus" (thin lines) model is shown together with the observed angular correlation function of the B_{435}–band dropouts. The two models describe the observed correlation function equally well ($\chi^2_{1+} = 0.97$ and $\chi^2_{ppl} = 0.91$). Right panel: the mean occupation number $\langle N_g \rangle$ predicted from the two best–fit HOD models is shown as a function of mass. Halo mass is in units of $h^{-1}M_\odot$. The two models predict similar $\langle N_g \rangle$ values in the mass range of $10^{12} - 10^{13}\ h^{-1}M_\odot$, to which most of the massive halos "observed" in the data most likely belong. This implies that our estimate is very robust regardless of the employed HOD model in the high–end of the halo mass function. However, at the mass scale of $M > 10^{13}h^{-1}M_\odot$, $\langle N_g \rangle$ from the "one–plus" model largely exceeds the other. On the other hand, at $M < 10^{11}h^{-1}M_\odot$, the "pure power–law" model implies a larger number of low–mass halos in the samples, while the "one–plus" model is truncated (by definition; see text for further discussion).

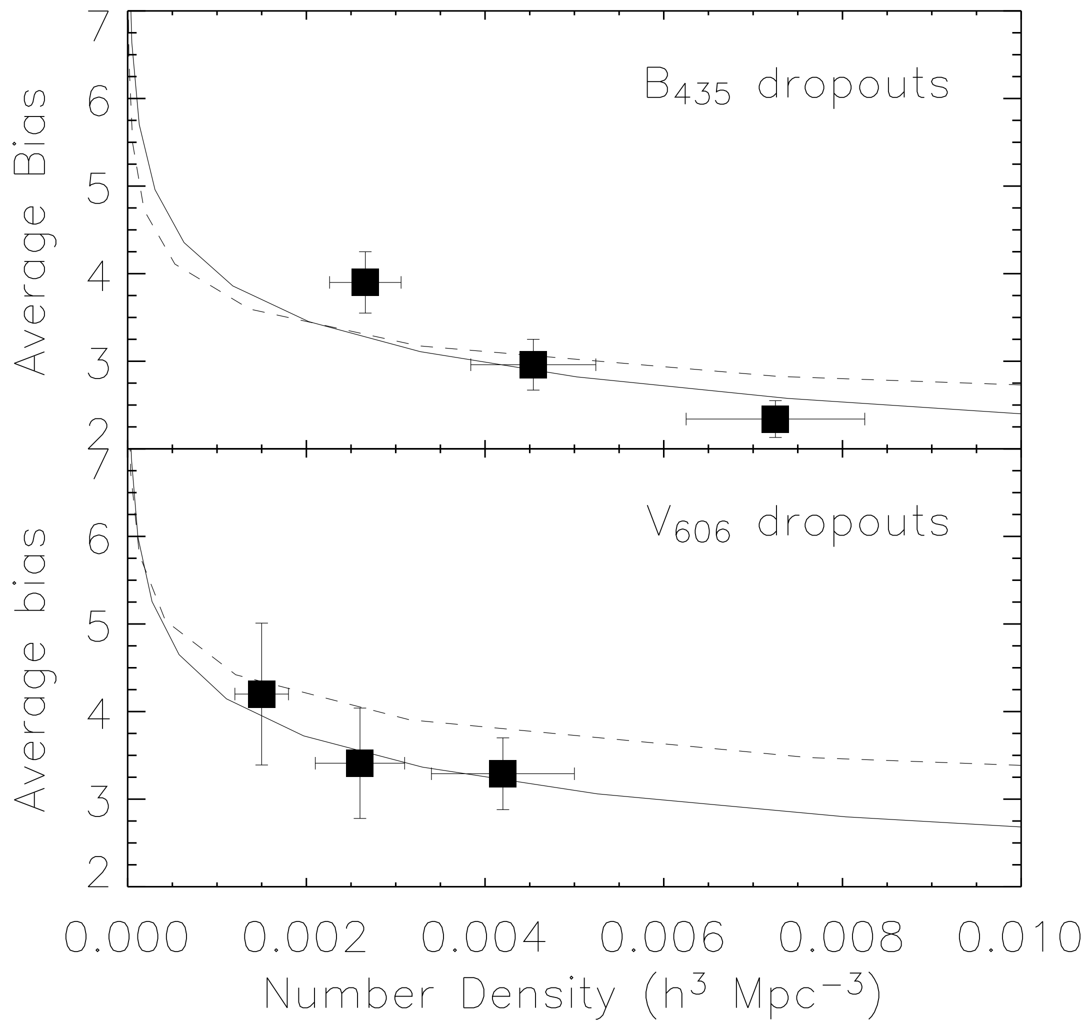

Fig. 9.— The average bias vs the galaxy (or halo) abundance: The data points and the solid lines represent the average galaxy bias from the correlation measures and the predictions as a function of galaxy number density, respectively. The average bias is computed as linear bias (Sheth & Tormen 1999) weighted by the best–fit HOD to account for the galaxy multiplicity. The dashed lines show the average halo bias as a function of halo number density. If there were one–to–one correspondence between halos and galaxies, then the two would coincide.

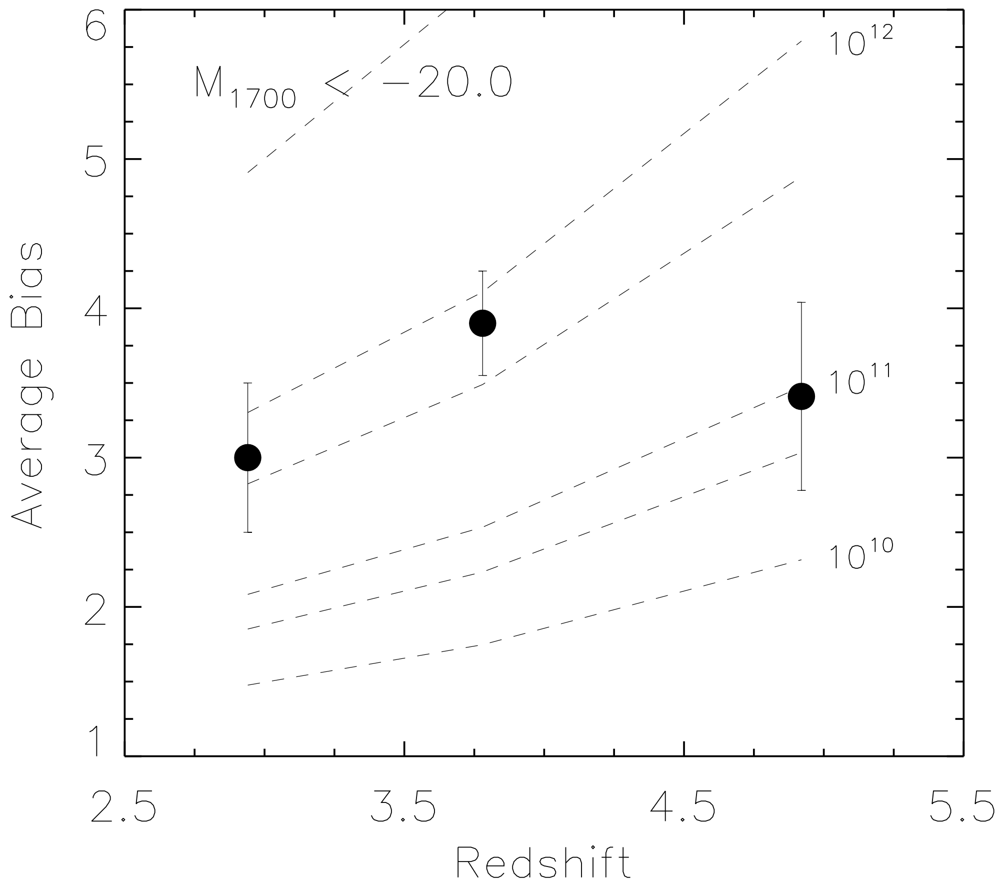

Fig. 10.— The evolution of the average bias as a function of redshift: the data points indicate the average bias implied for the U, B_{435} and V_{606}–band dropouts at the fixed absolute luminosity threshold $M_{1700} \leq -20.0$, which corresponds to $\mathcal{R} \leq 25.5$ at $z \sim 3$. The dashed lines show the predicted linear bias from the Sheth & Tormen (1999) model for halo mass $M_{halo} \geq M_{min} = 10^{10}, 5 \times 10^{10}, 10^{11}, 5 \times 10^{11}, 10^{12}$ and 5×10^{12} $h^{-1}M_{\odot}$ (from bottom). At $z \sim 3$ and 4, the observed galaxies are hosted by dark halos of similar mass ($5 \times 10^{11} h^{-1}M_{\odot}$ – 10^{12} $h^{-1}M_{\odot}$). At $z \sim 5$, the observed clustering strength of the galaxies implies that they are hosted by less massive halos, $M_{halo} \sim 10^{11} h^{-1}M_{\odot}$. This suggests that star–formation may have been more efficient at $z \sim 5$.

Table 1: The space–based data set

Field	A[a]	$\sigma(B_{435})$[b]	$\sigma(V_{606})$[b]	$\sigma(i_{775})$[b]	$\sigma(z_{850})$[b]	$N_{LBG,4}$[c]	$N_{LBG,5}$[c]
GOODS–N	160.0	29.00	29.08	28.33	28.09	1169	502
GOODS–S	160.0	28.88	29.05	28.34	28.06	1294	376

[a]Survey area, in units of arcmin^2

[b]1 σ surface brightness fluctuations within 1 arcsec^2 apertures

[c]Number of B_{435}/V_{606}–band dropout Lyman–break galaxies

Table 2: The ground–based data set

Field	A	$\sigma(U)$[a]	$\sigma(B)$[a]	$\sigma(R)$[a]	N_U[b]
extended GOODS–S	1200	29.42	29.75	28.95	1609

[a]1 σ surface brightness fluctuations within 1 arcsec^2 apertures

[b]Number of U–band dropout Lyman–break galaxies ($R \leq 25.5$)

Table 3: The LBG abundance, the angular correlation function and the inferred correlation lengths

Flavor	Sample	$n_g(\times 10^{-3})$	$A_{w,0}$	β_0	$r_{0,0}$	$A_{w,1}$	β_1	$r_{0,1}$
U	$R \leq 25.5$	3.3 ± 1.0	$0.56^{+0.04}_{-0.04}$	0.6	$4.1^{+0.1}_{-0.2}$	$0.52^{+0.28}_{-0.20}$	$0.63^{+0.11}_{-0.12}$	$4.0^{+0.2}_{-0.2}$
U	$R \leq 24.5$	0.7 ± 0.3	$1.16^{+0.06}_{-0.08}$	0.6	$6.5^{+0.2}_{-0.3}$	$0.54^{+0.23}_{-0.16}$	$0.44^{+0.08}_{-0.08}$	$6.4^{+0.3}_{-0.3}$
U	$R \leq 24.0$	0.2 ± 0.1	$1.58^{+0.14}_{-0.17}$	0.6	$7.8^{+0.4}_{-0.5}$	$0.84^{+0.68}_{-0.32}$	$0.52^{+0.12}_{-0.11}$	$7.8^{+0.5}_{-0.6}$
B_{435}	$z_{850} \leq 27.0$	7.3 ± 1.0	$0.38^{+0.04}_{-0.05}$	0.6	$2.9^{+0.2}_{-0.2}$	$0.42^{+0.32}_{-0.26}$	$0.69^{+0.16}_{-0.15}$	$2.8^{+0.2}_{-0.2}$
B_{435}	$z_{850} \leq 26.5$	4.5 ± 0.7	$0.60^{+0.10}_{-0.06}$	0.6	$3.9^{+0.3}_{-0.3}$	$0.75^{+0.56}_{-0.37}$	$0.70^{+0.17}_{-0.13}$	$3.7^{+0.3}_{-0.3}$
B_{435}	$z_{850} \leq 26.0$	2.7 ± 0.4	$0.99^{+0.14}_{-0.13}$	0.6	$5.3^{+0.4}_{-0.5}$	$0.64^{+0.98}_{-0.45}$	$0.64^{+0.19}_{-0.19}$	$5.1^{+0.4}_{-0.5}$
V_{606}	$z_{850} \leq 27.0$	4.2 ± 0.8	$0.76^{+0.13}_{-0.15}$	0.6	$4.4^{+0.5}_{-0.5}$	$1.00^{+1.68}_{-0.75}$	$0.85^{+0.20}_{-0.23}$	$4.2^{+0.4}_{-0.5}$
V_{606}	$z_{850} \leq 26.5$	2.6 ± 0.5	$1.12^{+0.34}_{-0.25}$	0.6	$5.8^{+1.1}_{-0.8}$	$2.08^{+8.80}_{-1.76}$	$1.10^{+0.30}_{-0.27}$	$4.4^{+0.7}_{-0.7}$
V_{606}	$z_{850} \leq 26.0$	1.5 ± 0.3	$1.70^{+0.42}_{-0.37}$	0.6	$7.5^{+1.1}_{-1.0}$	$3.88^{+12.89}_{-3.46}$	$1.10^{+0.31}_{-0.29}$	$5.3^{+1.1}_{-1.0}$

Note. — The number density (n_g) and the comoving correlation lengths (r_0) are in units of h^3 Mpc^{-3} and h^{-1} Mpc, respectively. The quantities with the secondary subscript "0" are when the slope is fixed to a fiducial value $\beta = 0.6$, those with the subscript "1" are when both β and A_w are allowed to vary.

Table 4: The best–fit HOD parameters[a] , the ratio of galaxy number density to halo number density $\langle N_g \rangle_M$, and the average halo mass $\langle M \rangle$[b] for different luminosity thresholds

Flavor	Sample	M_1[b,c]	α[c]	$\langle N_g \rangle_M$	$\langle M \rangle$[b]
B_{435}	$z_{850} \leq 27.0$	1.3×10^{12}	0.65	0.31±0.14	$(4\pm1)\times10^{11}$
B_{435}	$z_{850} \leq 26.5$	1.3×10^{12}	0.65	0.38±0.13	$(6\pm1)\times10^{11}$
B_{435}	$z_{850} \leq 26.0$	1.3×10^{12}	0.65	0.49±0.13	$(8\pm2)\times10^{11}$
V_{606}	$z_{850} \leq 27.0$	1.0×10^{12}	0.80	0.20±0.18	$(2\pm1)\times10^{11}$
V_{606}	$z_{850} \leq 26.5$	1.0×10^{12}	0.80	0.24±0.19	$(3\pm1)\times10^{11}$
V_{606}	$z_{850} \leq 26.0$	1.0×10^{12}	0.80	0.30±0.21	$(4\pm2)\times10^{11}$

[a]Using the "pure power–law" model

[b]All masses are in units of $h^{-1}M_\odot$

[c]Note that the same HOD parameters, M_1 and α, constrained from the full sample, were used for all sub–samples